

The Bolocam Galactic Plane Survey: Survey Description and Data Reduction

James Aguirre¹, Adam Ginsburg², Miranda Nordhaus³, Meredith Drosback⁴, John Bally², Cara Battersby², Eric Todd Bradley⁵, Claudia Cyganowski⁶, Darren Dowell⁷ Neal J. Evans II³, Jason Glenn², Paul Harvey^{3,2}, Erik Rosolowsky⁸, Guy S. Stringfellow², Josh Walawender⁹, and Jonathan Williams¹⁰

¹*Department of Physics and Astronomy, University of Pennsylvania, Philadelphia, PA*

jaguirre@sas.upenn.edu

²*CASA, University of Colorado, CB 389, Boulder, CO 80309*

³*Department of Astronomy, University of Texas, 1 University Station C1400, Austin, TX 78712*

⁴*Department of Astronomy, University of Virginia, P.O. Box 400325, Charlottesville, VA 22904*

⁵*Department of Physics, University of Central Florida*

⁶*Department of Astronomy, University of Wisconsin, Madison, WI 53706*

⁷*Jet Propulsion Laboratory, California Institute of Technology, 4800 Oak Grove Dr., Pasadena, CA 91104*

⁸*Department of Physics and Astronomy, University of British Columbia, Okanagan*

⁹*Institute for Astronomy, University of Hawaii, 640 N. Aohoku Pl., Hilo, HI 96720*

¹⁰*Institute for Astronomy, University of Hawaii, 680 Woodlawn Drive, Honolulu, HI 96822*

ABSTRACT

We present the Bolocam Galactic Plane Survey (BGPS), a 1.1 mm continuum survey of 150 square degrees of the Galactic Plane in the 1st, 2nd, and 3rd quadrants. The BGPS represents the first large area, systematic survey of the Galactic Plane in the (sub)millimeter continuum without pre-selected targets. The survey has detected 10^4 clumps to a limiting depth of between 20 and 50 mJy

RMS. This paper details the survey observations and methods. We treat carefully the comparison of the survey pointing and flux calibration and serves as a companion to the public data release through NASA’s Infrared Processing and Analysis Center (IPAC). We anticipate that the BGPS will be useful as a finder chart for ALMA and as a long-wavelength complement to *Herschel*-HiGAL.

Subject headings: ISM: - molecular clouds – stars: formation – high mass millimeter continuum

1. Introduction

Millimeter-wavelength continuum surveys of the Galactic plane provide the best way to identify high-column density clumps and clumps where planets, stars, and star clusters form. Such data can locate and lead to the measurement of the physical properties of clumps un-biased by selection effects such as the presence of embedded stars, star clusters, infrared sources, masers, or radio continuum emission. Galaxy-wide surveys are essential for measuring the impacts of the environment on clump properties and star formation activity. Do clump properties vary with location in or out of spiral arms? Do clump properties vary with Galactocentric distance? Do they depend on the level of nearby star formation activity? Galactic plane surveys of mm-wavelength dust continuum emission provide the most efficient tool for the identification of potential or active sites of star formation, including the rare objects where the most massive stars and cluster are, or soon will be, forming. Dust continuum surveys of the Galaxy provide essential “ground truth” required for the analysis of distant galaxies where individual clouds and clumps are not resolved and only galaxy-wide average quantities can be measured.

Dust continuum emission near a wavelength of 1 mm is the best tracer of the material most directly associated with the formation of planetary systems, stars, and star clusters (Johnstone & Bally 2006). Galactic dust continuum radiation at this wavelength is optically-thin almost everywhere, and at typical dust temperatures of order 10 K or more, is observed on the Rayleigh-Jeans tail of the Planck function. Thus, the determination of column densities is relatively straight forward if the dust temperature is known.

A crucial step in the observational study of star and cluster formation is identification and characterization of the cloud clumps which will soon form or are actively forming stars. Massive stars and clusters form from high-density cloud clumps with very large column densities and extinctions $A_V > 100$. Thus, such cloud clumps are best investigated at millimeter and sub-millimeter wavelengths. However, the interpretation of various gas tracers

that produce emission lines in this portion of the spectrum is very difficult. Although in principle, spectral lines provide excellent diagnostics of line-of-sight motions, temperatures, and densities in a cloud, variations in tracer abundances caused by depletions and complex chemical processing, uncertainties in excitation conditions, and the impacts of radiation fields and shocks make the derivation of column densities, masses, and other physical properties of cloud clumps very difficult. The continuum emission from warm dust provides a more reliable tracer of the column densities and clump masses.

The advent of focal plane arrays containing hundreds of individual bolometers sensitive to millimeter and sub-millimeter (sub-mm) radiation has enabled large-scale surveys of mm-wavelength continuum emission from Galactic interstellar dust. The great advantage of continuum observations at 1.1mm is that the mass column density does not depend strongly on the dust temperature T_d (varying only linearly unless T_d is less than about 10 K) and is independent of the gas volume density. Using the same dust opacity as Enoch et al. (2006) and Young et al. (2006), and assuming a gas-to-dust mass ratio X of 100, the mass sensitivity can be written as

$$M_{\text{gas}} \approx 0.22 \left(e^{12.9/T_d} - 1 \right) \left(\frac{S_\nu}{15 \text{ mJy}} \right) D_{\text{kpc}}^2 M_\odot \quad (1)$$

where D_{kpc} is the distance to the source in kpc. (At $S_\nu = 15$ mJy this corresponds to an RMS extinction sensitivity of $A_V \sim 1$ mag, with the same T_d dependence). It is thus possible with a wide area, relatively shallow 1.1 mm survey to provide an unmatched, uniform inventory of massive star-forming and starless condensations.

This survey presents the results of one of the first wide-area, untargeted surveys of the Galactic Plane in the millimeter continuum. We have used the 144 element Bolocam focal plane array, mounted at the Cassegrain focus of the 10 meter diameter sub-mm telescope at the Caltech Sub-millimeter Observatory (CSO), to survey over 150 square degrees of the northern Galactic plane at a wavelength of 1.1 mm in the dust continuum. Figure 1 shows the coverage of the BGPS. Maps of the entire BGPS are presented in Figure 1. We have detected 10^4 clumps in the surveyed fields, providing an unbiased sample of clumps suitable for multi-wavelength and high-resolution studies with existing telescopes and future facilities. The clump catalog is described in a companion paper (Rosolowsky et al. 2009).

The outline of the paper is as follows. Section 2 describes the instrument and the observations. Section ?? describes the flux calibration and errors. Section ?? describes the construction of an absolute reference frame for the observations and verification against

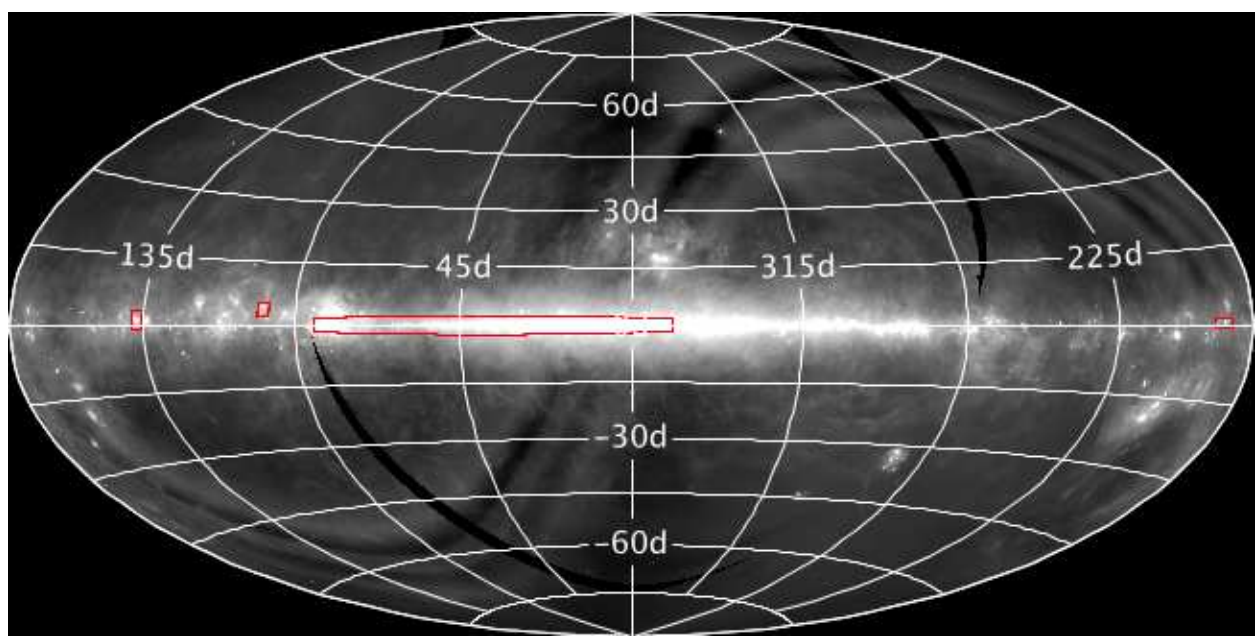


Fig. 1.— The coverage of the BGPS. The background greyscale is IRAS 100 μm .

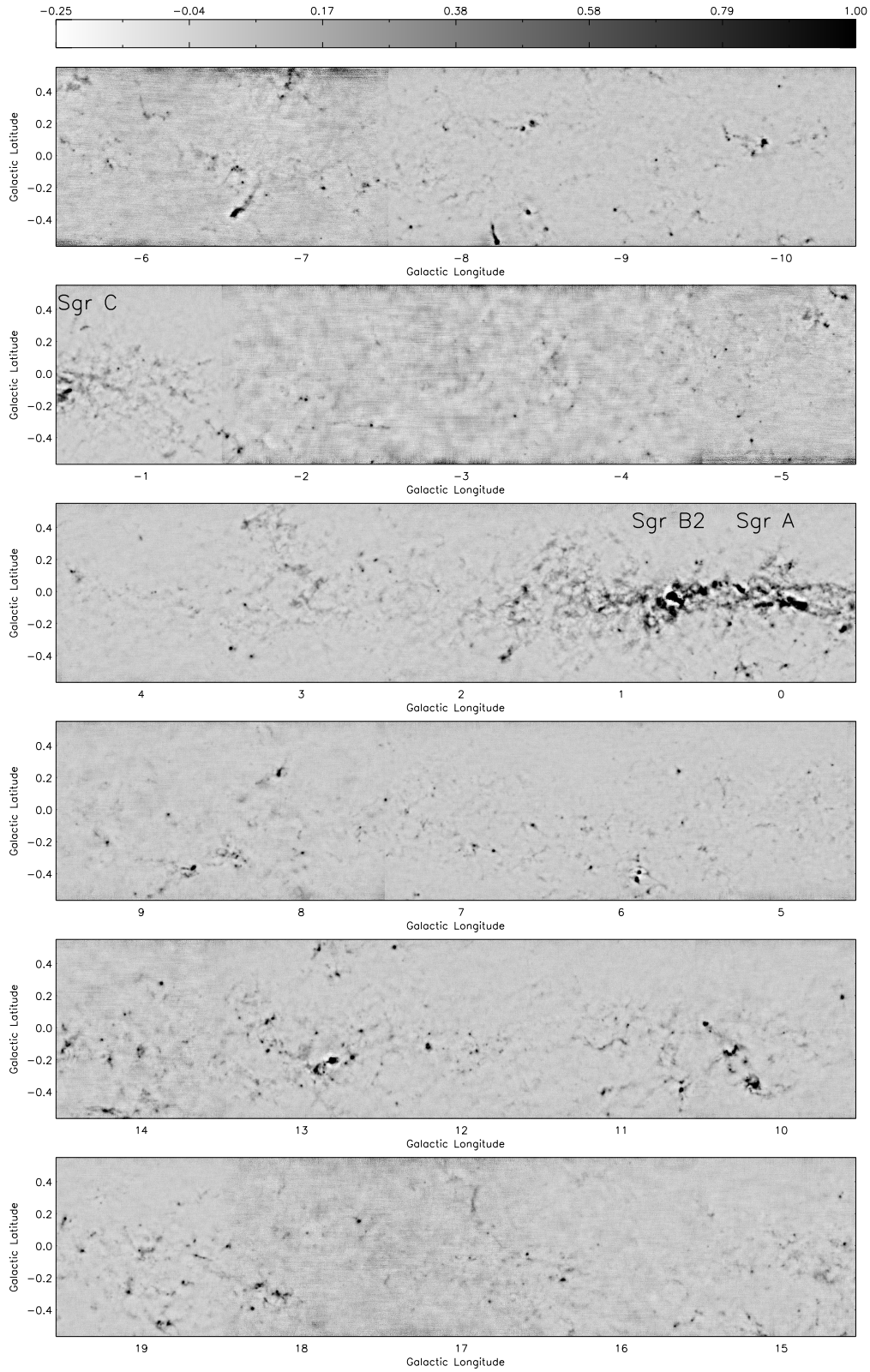


Fig. 2a.— $l = -10.5$ to $l = 19.5$ Units are Jy/Beam. The brightest sources, e.g. Sgr B2, Sgr A, and sources near $l = 10$ and $l = 13$, appear to be saturated, but this is only a display artifact. The noise is more pronounced from $l = -7$ to $l = -2$ because this region was observed less.

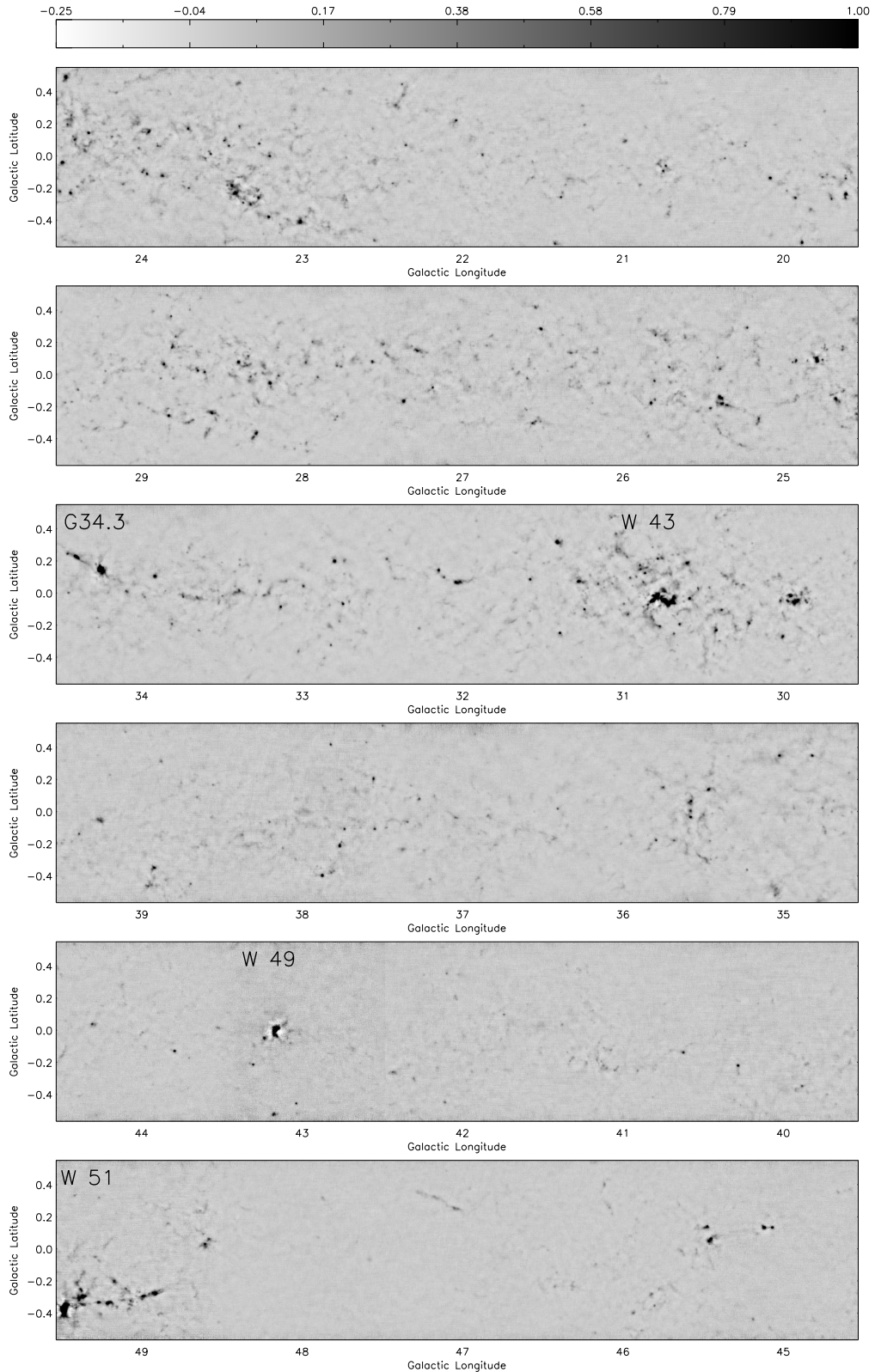


Fig. 2b.— $l = 19.5$ to $l = 49.5$. Units are Jy/Beam . G34.3+0.15, W 51, W 43, W 49, and M 17 appear to be saturated, but this is only a display artifact

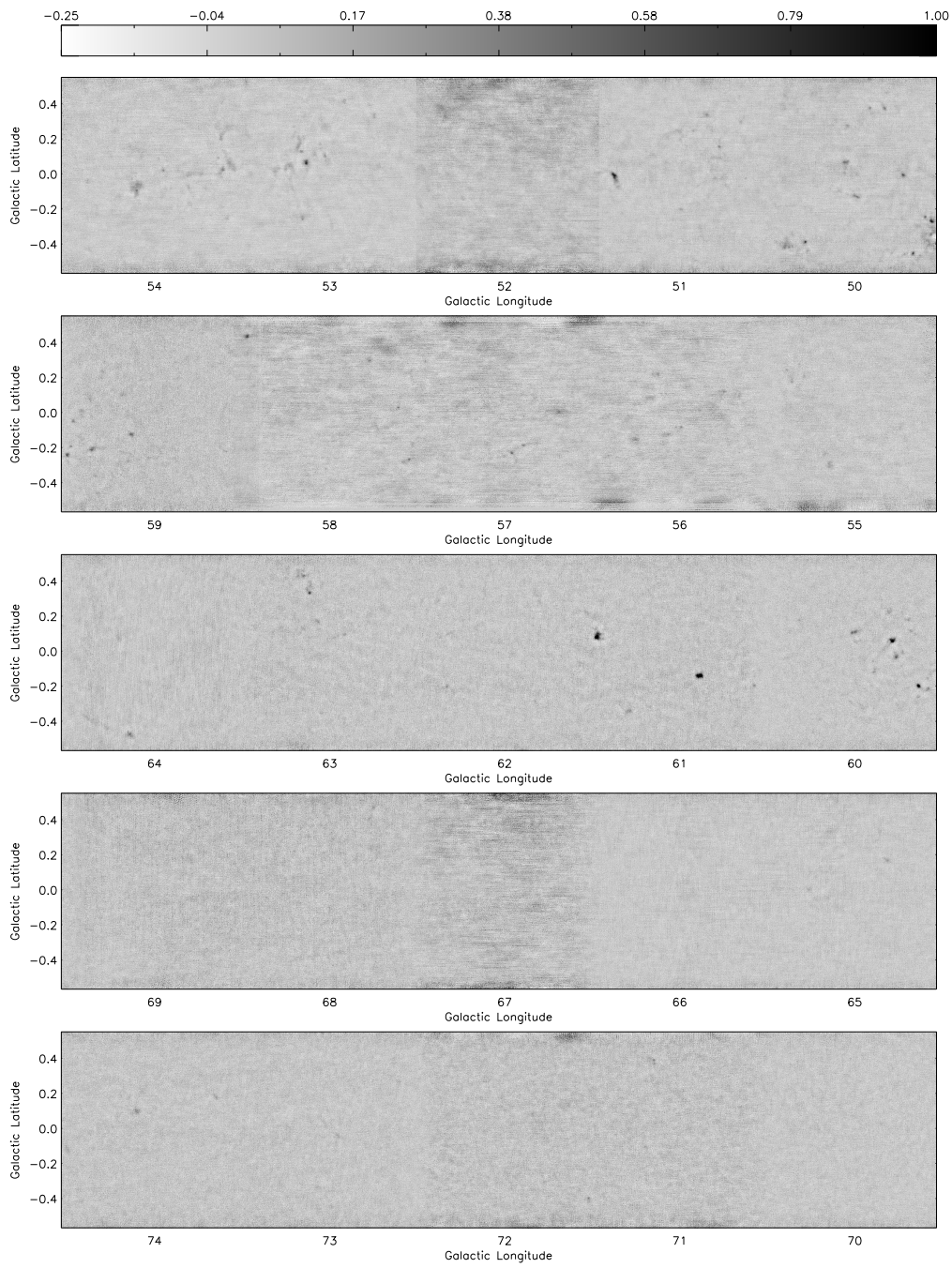


Fig. 2c.— $l = 49.5$ to $l = 74.5$.

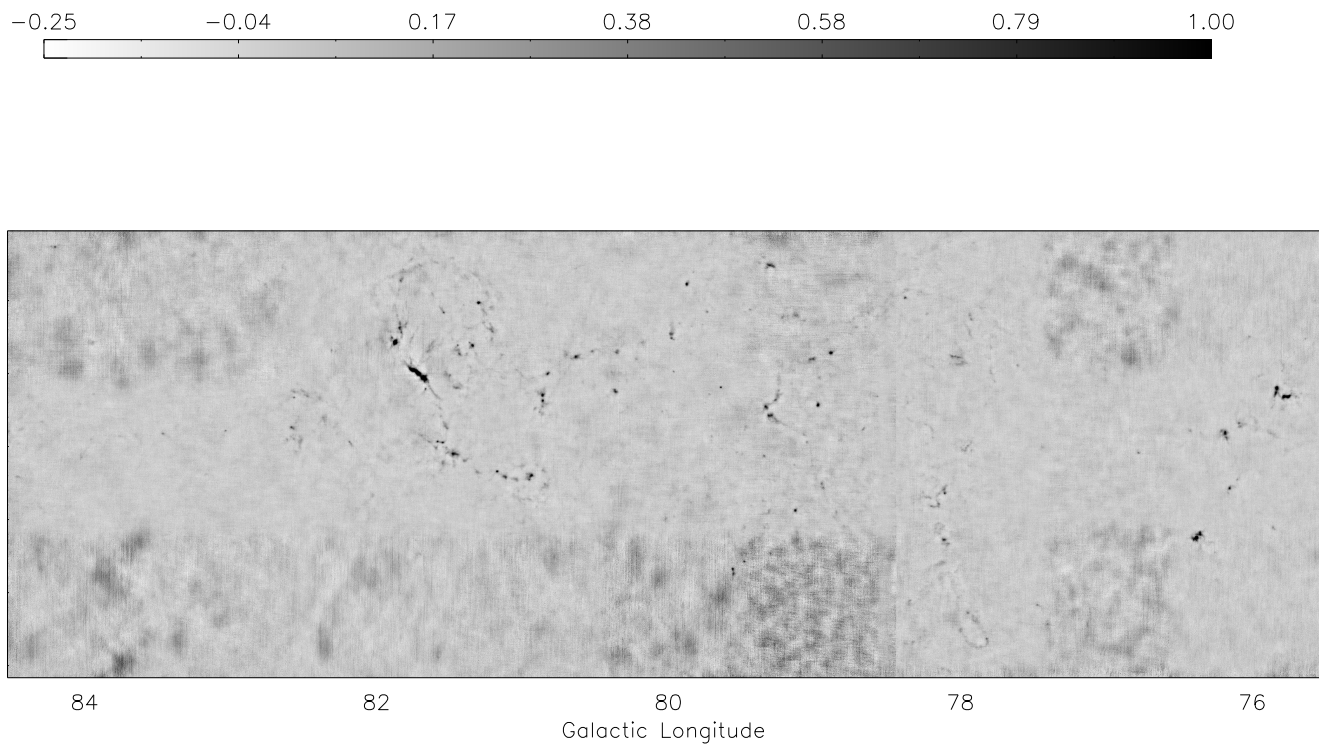


Fig. 2d.— The Cygnus Arm.

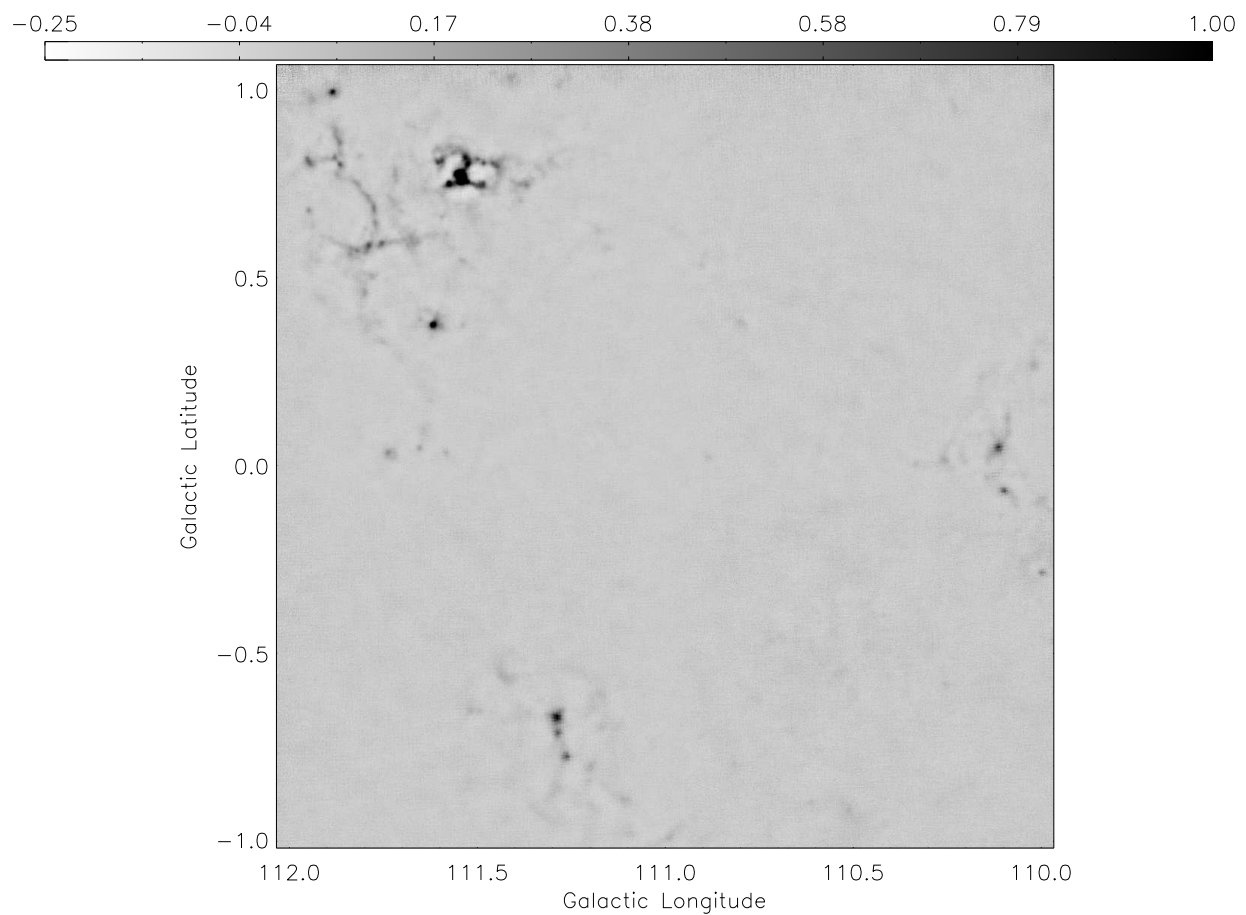


Fig. 2e.— Cloud complexes centered at $l = 111$ in the Perseus Arm.

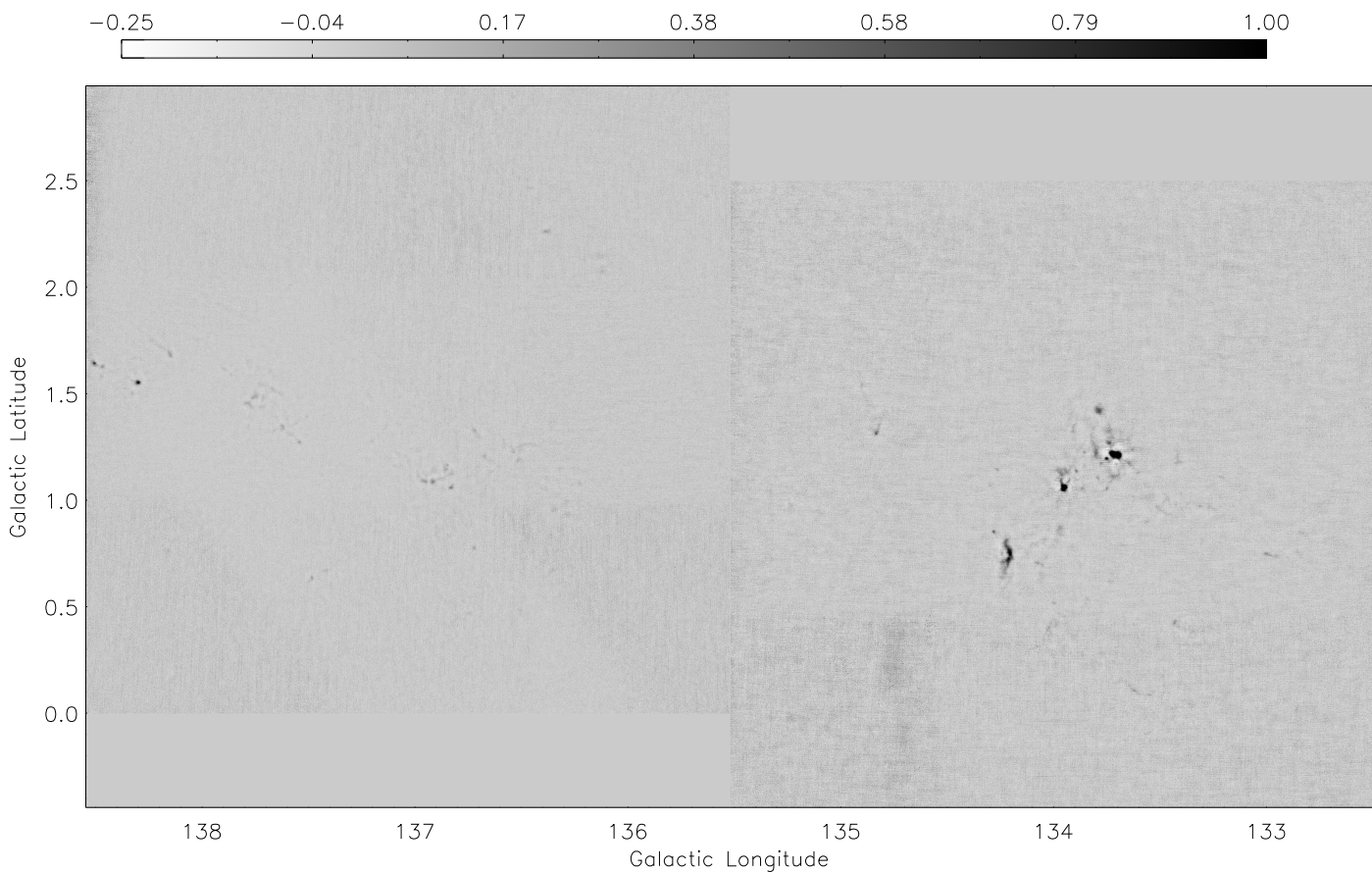


Fig. 2f.— W3/4/5

2. Observations

Bolocam¹ is the facility 144-element bolometer array camera operating from the 10.4 m dish of the Caltech Submillimeter Observatory (CSO) on the summit of Mauna Kea. We used the filter configuration with a bandcenter of 268 GHz (hereafter 1.1 mm) and fractional bandwidth $\Delta\nu/\nu = 0.17$. The passband is constructed to exclude the $^{12}\text{CO}(2 \rightarrow 1)$ emission line. Figure 3 shows the passband. We compute color corrections for sources of varying spectral index in Appendix A.

The array field-of-view is $7'.5$, with individual detectors having nearly Gaussian beams of $31.2''$ FWHM. The spacing of the pixels at 1.1 mm is $1.6f\lambda$, so the focal plane is not instantaneously sampled. The Bolocam instrument is described in greater detail in Haig et al. (2004) and Glenn et al. (2003).

The observations described here were acquired during six separate observing sessions at the CSO over the course of two years. The observing epochs are given in Table 1, along with corresponding ranges for the zenith opacity τ_{225} of the CSO tipper tau. Because of the CSO weather multiplexing policy, Bolocam observations were typically scheduled when $\tau_{225} > 0.06$. Between each observing epoch, Bolocam was removed from its mount at the re-imaged Cassegrain focus and stored warm. Thus the flux calibration and pointing model must be re-computed for each epoch to allow for changes in the instrument and optics.

Our basic observing strategy was to raster scan Bolocam by moving the primary mirror of the CSO to modulate the astrophysical signal faster than fluctuations in atmospheric opacity. Each field was scanned with alternating raster scans along l and b . Starting with Epoch III, the fundamental scan unit was a $3^\circ \times 1^\circ$ block. Each block was scanned with 23 scans along lines of constant b , and 67 scans along lines of constant l . In both cases, the spacing between adjacent rasters was $162''$. The total time for such a scan was between 39 and 48 minutes. In order to fill in the instantaneously undersampled focal plane, we began using in Epoch II a field rotator to mechanically align the focal plane at an optimal orientation along the scan direction to improve the sampling orthogonal to the scan direction. This is shown in Figure 4. The data were electronically sampled at 10 Hz along the scan direction, slightly higher than the Nyquist rate for the scan speed of $120'' \text{ s}^{-1}$. Without the field rotator, the coverage shows variations of 100% from pixel to pixel in a single raster of a field. With the rotator

The resulting coverage using the above scan pattern and the field rotator, is typically uniform to

¹<http://www.cso.caltech.edu/bolocam>

with only a single pass across the field.

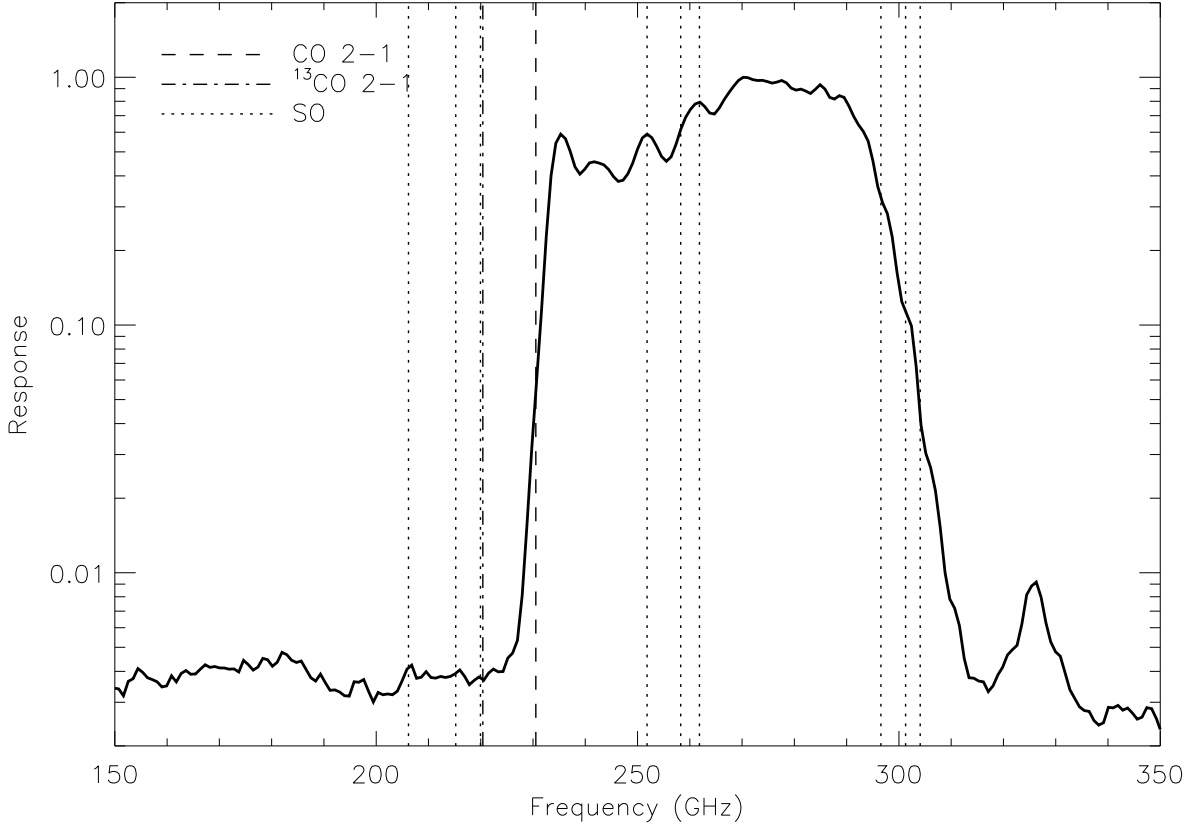


Fig. 3.— The Bolocam 1.1 mm bandpass. Bright molecular emission lines are shown at their rest frequencies. Note that the Bolocam passband rejects > 90% of the ^{12}CO flux, leaving our continuum measurements largely uncontaminated. SO and CH₃OH lines are probably the dominant contributors to line flux in the passband. Nummela et al. (1998) found that 22% of the flux in one pointing towards Sgr B2 was from lines, and Yoshida & Phillips (2005) reported > 40% in Orion A from line emission

3. Flux Density and Surface Brightness Calibration

The absolute flux calibration is obtained from observations of Mars and Uranus (the “primary calibrators”). The millimeter-wave flux of these planets is known to $\sim 5\%$ (Orton et al. 1986; Griffin & Orton 1993). Calibrations at (sub)millimeter wavelengths are strongly affected by atmospheric opacity corrections. Further, the detector responsivity of Bolocam’s

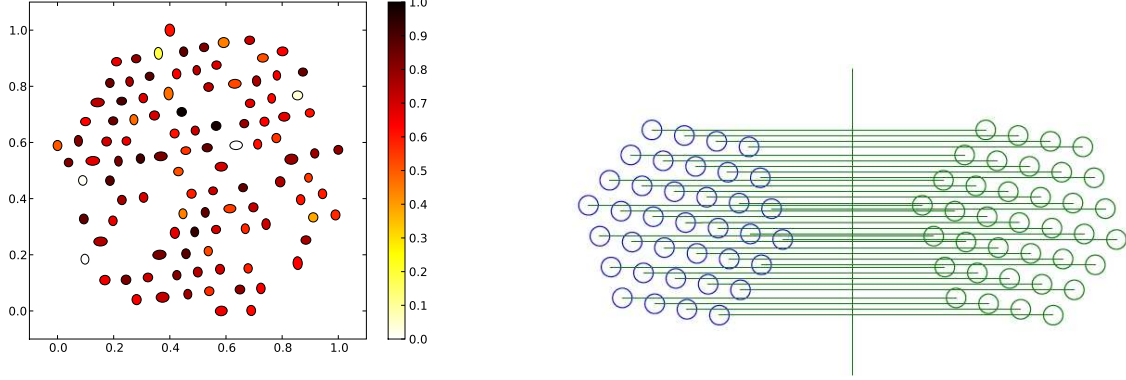


Fig. 4.— Left: the position, ellipticity and relative response of the detectors in the Bolocam focal plane as mapped to the sky. Right: The effect of field rotation on the coverage obtained via Bolocam raster scans.

bolometers is a non-linear function of the mean atmospheric loading.

To relate observations of the primary calibrators to observations of the BGPS fields, we make use of the following relation. The calibration \mathcal{S} , referred to the detectors, is given by

$$\mathcal{S} \left[\frac{\text{V}}{\text{Jy}} \right] = S(\tau) \eta A \exp(-\tau) \Delta\nu \quad (2)$$

where S is the bolometer responsivity ([V/W]), η is the system optical efficiency, A is the effective telescope collecting area, $\Delta\nu$ is the bandwidth, and τ is the line-of-sight, in-band atmosphere opacity. Under the assumption that the only power variation on the detectors is due to the power from the atmosphere, which may be parameterized by τ , \mathcal{S} is a single-valued function of τ . We have used the mean bolometer resistance as a proxy for τ , since

Table 1. Observing Epochs for the BGPS

Begin (UT)	End (UT)	Nights	τ_{225}
2005 Jul 03	2005 Jul 13	5	0.1
2005 Sep 04	2005 Sep 12	5	0.1
2006 Jul 01	2006 Jul 13	5	0.1
2006 Sep 01	2006 Sep 09	5	0.1
2007 Jul 01	2007 Jul 13	5	0.1
2007 Sep 01	2007 Sep 09	5	0.1

the bolometer resistance is a single-valued function of loading. *This quantity is monitored continuously for all observations.* Note that this calibration curve folds in both the effects of changing atmospheric transmission, as well as changes in the detector response with optical loading.

A fit to the observed values for the primary calibrators was performed for each epoch separately. The agreement between epochs was good, so a single combined calibration was used for all data here. The calibration curve is shown in Figure 5. The resulting error on the calibration curve fit is less than 5% (statistical) over the observed range of τ . A tally of all contributions to the flux density error is given in Table 2.

The above flux density calibration only accounts for the average calibration of bolometer Volts to Janskys. It is also necessary to account for the variation of bolometer response across the focal plane. We do this by monitoring the response to the atmosphere emission in all bolometers. Since the atmosphere is common to all detectors, any changes in response are due to the intrinsic properties of the detectors. The change in relative response with loading for a typical detector is shown in Figure 5. The actual application of the method to the time series of the bolometer data is shown in Figure 6, and is discussed further in Section 5.

The instrument beam size (PSF) is measured using the planets Uranus and Neptune which are nearly point sources for Bolocam. The maps of the planets, including all detectors, are fit to a Gaussian profile. The beam area is that averaged over all detectors, and is $?1.71 \times 10^{-6} \text{ TBD}$ (35.6'') steradians. This allows conversion of the maps, calibrated in Jy beam^{-1} , into surface brightness (MJy sr^{-1}). The uncertainty in the beam size is $?7\% \text{ TBD}$ (number quoted is the uncertainty in the mean beam size), leading to an uncertainty in the surface brightness calibration of **TBD**.

3.1. Comparison to Other Surveys

Comparison of the accuracy of the Bolocam flux density calibration with the SCUBA 850 μm results is complicated by the unknown effect of the dust spectral index. However, there are several large-area surveys with the MAMBO instrument at 1.2 mm with which we can compare. Figure 7 shows the comparison of fluxes extracted from our map in the Cygnus Arm with those of Motte et al. (2007).

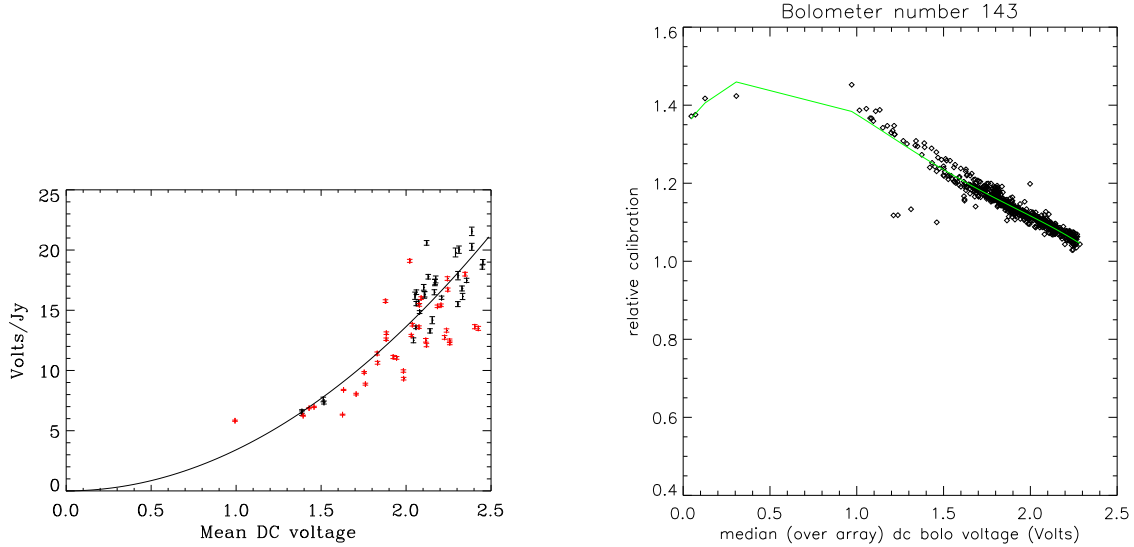


Fig. 5.— Left: Average calibration curve [V/Jy] versus the mean detector voltage, a proxy for atmospheric loading. Red points are observations of Mars and black of Uranus. Right: Scaling of the relative calibration with atmospheric loading for bolocam 143. *To be replaced with new figure*

4. Astrometry

4.1. Absolute Reference Sources and Pointing Model

We constructed an absolute reference system for the BGPS by observing bright quasars and blazars near the Galactic Plane. The distribution of sources over the sky is shown in Figure 8 and the list is given in Appendix C.

Pointing observations were performed approximately once every two hours over the night. These sources were then mapped in alt/az coordinates relative to the nominal telescope boresight. The elevation offsets showed a deviation from zero which was empirically well-modeled by a quadratic function of elevation and a linear function of azimuth. No systematic deviation was observed for the azimuth offsets.

Because the Galactic Plane appears over much of the sky, the pointing model necessarily encompasses a large range of elevation and azimuth. Nevertheless, an RMS scatter of $\sim 6''$ for the model over the entire observed range was achieved, with the scatter somewhat worse at the highest ZA. A separate model was constructed for each epoch. The residuals are nearly Gaussian, with an RMS of $\sim 6''$.

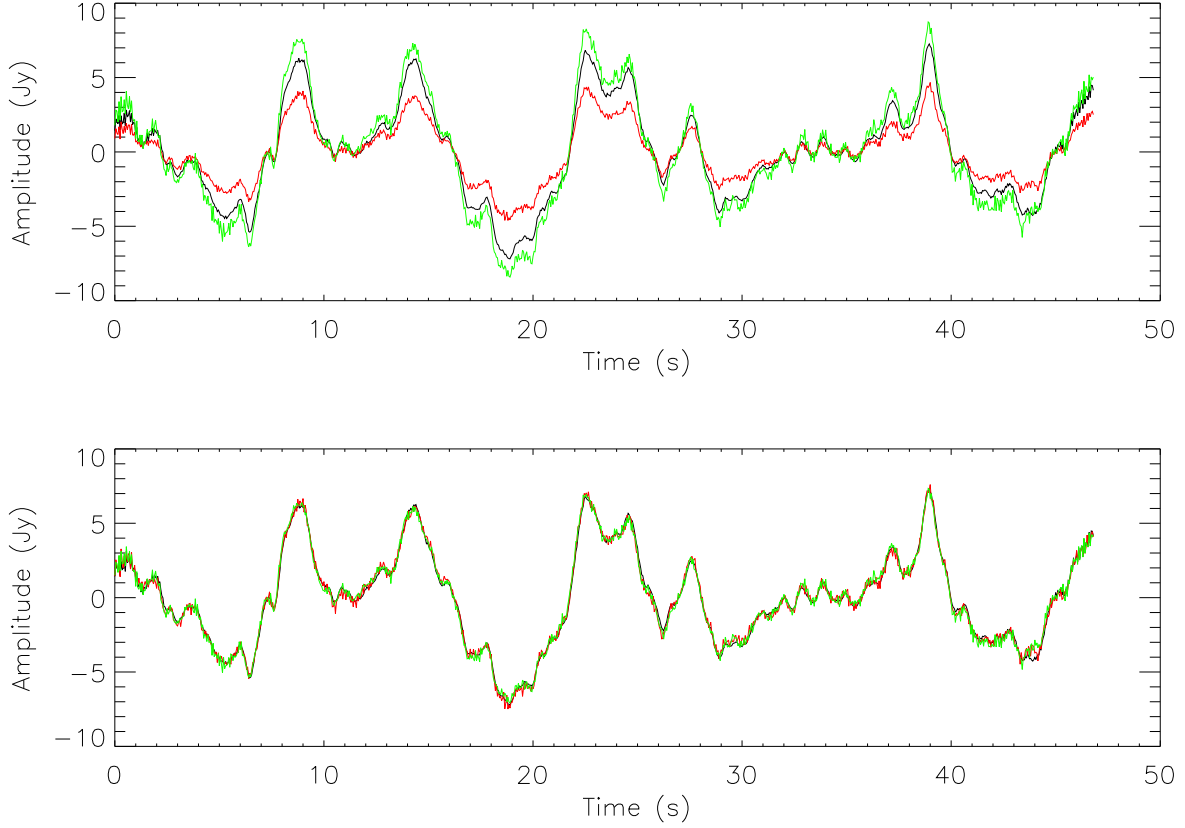


Fig. 6.— An illustration of the relative sensitivity calibration using the atmosphere as a calibrator. Black is the median over all bolometers (the atmosphere model), red and green are individual bolometers. a. before and b. after applying the relative calibration. Note the improved agreement.

Further details of the pointing calculation are given in Appendix B.

4.2. Pixel Positions in the FOV

In addition to the model for the pointing center, it is necessary to empirically determine actual projected pattern of the array on the sky, and measure the offset angle between the focal plane and the sky coordinate system. This is done by making observations which track all detectors across a bright source (a planet) and making maps from each bolometer individually.

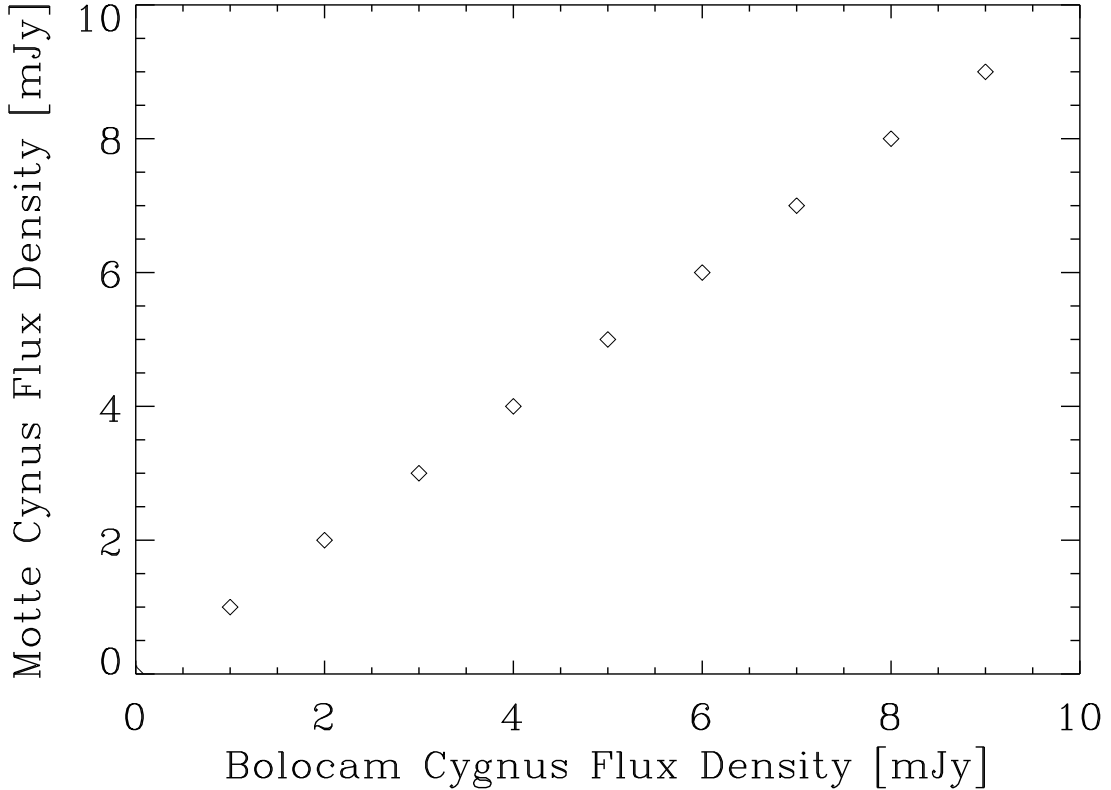


Fig. 7.— A comparison of the fluxes extracted in the same aperture from the Motte et al. (2007) MAMBO map and the Bolocam map of this paper.

A mean focus offset for the secondary is determined once per observing run. An elevation-dependent correction is applied via a CSO-determined look-up table between raster scans. We do not see any evidence that more frequent focus checks improve the quality of the PSF.

4.3. Relative Alignment and Mosaicing

Relative alignment was performed by finding the peak of the cross-correlation between images and a pointing master selected from the epoch with the best-constrained pointing model for that field. Each observation was initially mapped individually, then all observations of a given field were cross-correlated with a selected master image of that field. The cross-correlation peak was fit with a gaussian and the difference between the gaussian peak and

the image center was used as the pixel offset. The offsets were recorded and written to the timestreams. Finally, all observations of a field were merged into a single timestream with pointing offsets applied to create the field mosaic.

This method of alignment avoids the ambiguities inherent in using extracted sources to align fields, as the Bolocam sources are rarely point-like. It further avoids the pointing smearing and loss of peak flux density which would result if the the maps were coadded using the pointing model alone.

TBD: In low s/n fields, specifically $l=65$ to 75 , there was not enough signal to acquire a pointing offset using cross-correlation. In these fields the relative pointing offset is larger and the beam is slightly larger.

Show a cross-correlation map?

4.4. Comparison to SCUBA and SHARC-II Positions

The same cross-correlation procedure was used to compare to SCUBA maps where available. The morphological correlation between SCUBA and BGPS sources is excellent, so cross-correlation maps could be used to test our pointing model.

For the purposes of comparison with other surveys, we present in Appendix D a selection
Miranda's data here

Table 2. Flux density error budget

Source	Contribution
Pointing error uncertainty	2%
Calibration curve (Eq. 2) uncertainty	< 5%
PCA flux reduction uncertainty	4%
Absolute Mars flux uncertainty	5%
Beam size uncertainty (surface brightness)	X%
Total	7% (random) + 5% (systematic)

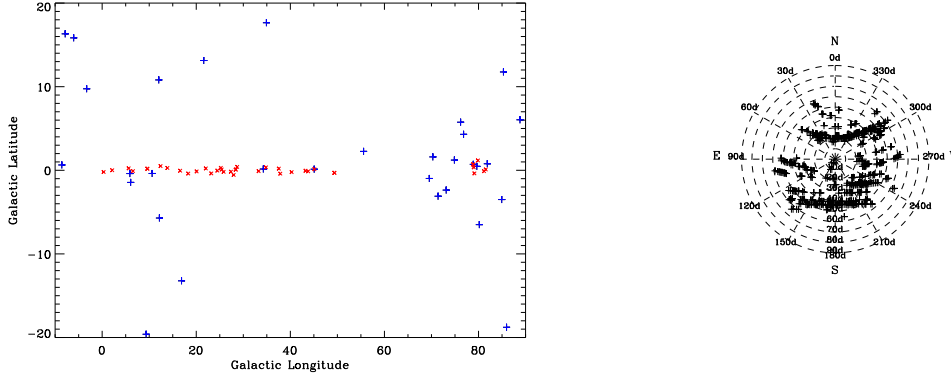


Fig. 8.— Left: The distribution of absolute reference sources (crosses) in the Galactic Plane (Appendix C). Also shown (crosses) are the locations of bright, isolated, compact sources for comparison with other surveys, as given in Appendix D. Right: The distribution of the pointing calibration sources across the local sky in Hawaii. Notice the good sampling of the entire region used for the Survey.

5. Mapping Algorithm

The essential signal-processing problem to be solved by the mapping algorithm is the estimation and removal of a signal due to fluctuating atmosphere emission which is $>\sim 100$'s of times stronger than the typical sources in our maps. We implement an iterative procedure for estimating both the atmosphere fluctuations and the astrophysical signal without *a priori* knowledge of either.

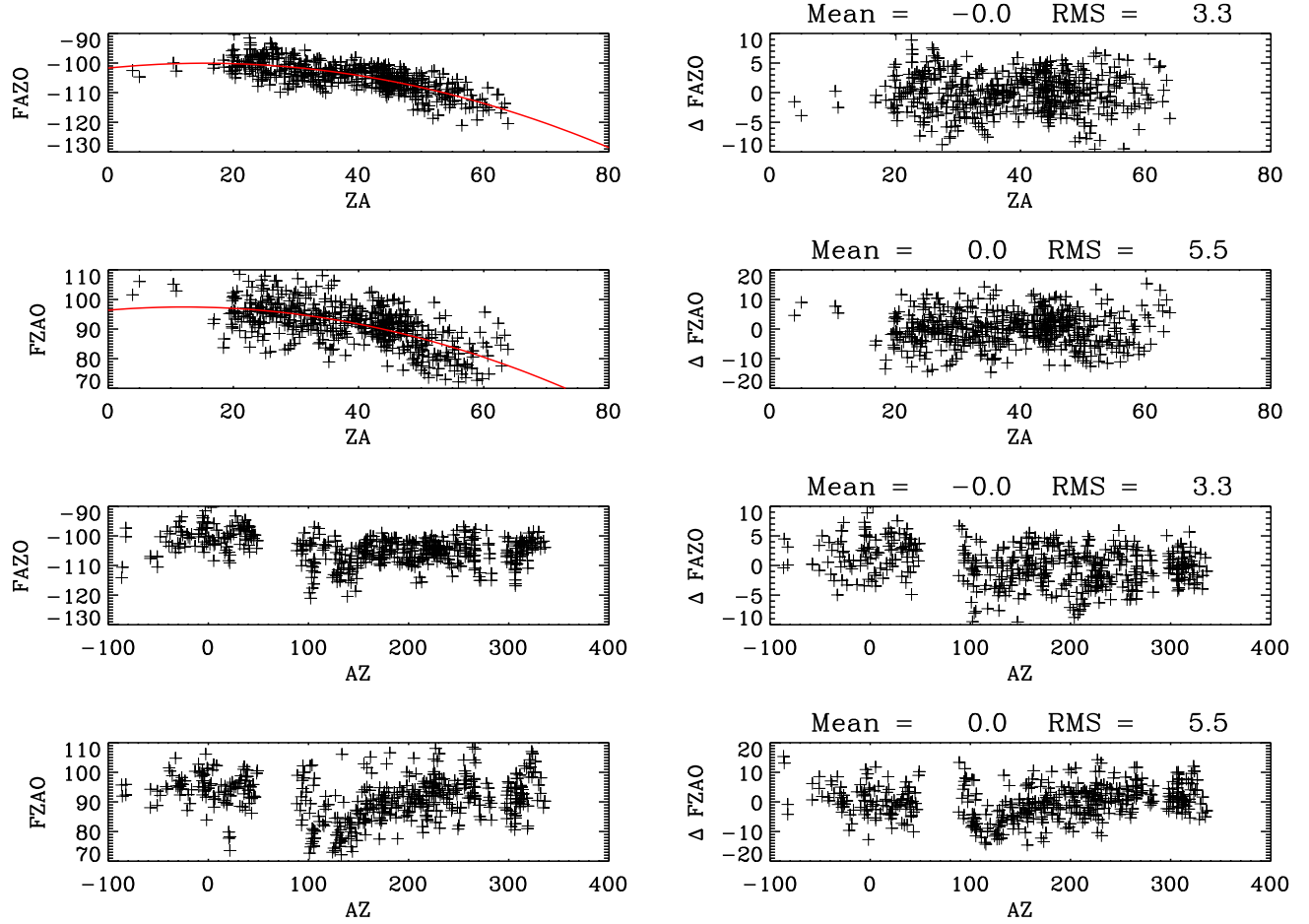
We assume the raw timestream data d for each bolometer (indexed by i) can be written as

$$d_i(t) = s_i(t) + a_i(t) + e_i(t) + \varepsilon_i(t) \quad (3)$$

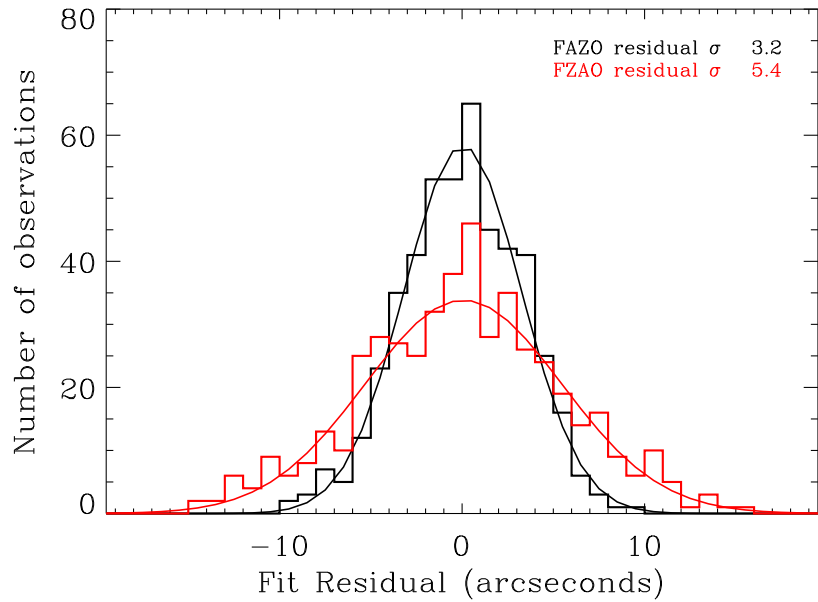
where s is the astrophysical signal, a is atmospheric fluctuation noise, e are non-random signals due to the instrument itself, and ε is irreducible Gaussian noise due to photon shot and detector noise. The process of making a maximum likelihood map in the presence of Gaussian noise is well-understood, and if the only contributions to the data were s and ε , then the minimum variance estimator of the true astrophysical map is given by

$$m = (A^T W A)^{-1} A^T W d \quad (4)$$

where A encodes the pointing information and W is the covariance matrix of the noise ε . Note that the mapping from data to map is a linear operator, $M = (A^T W A)^{-1} A^T W$. For compactness, Equation 4 will be written as $M[d] = m$. Note that the mapping operation is not invertible. However, note that given a map m , there exists a linear operation which



(a) The pointing model correction (left) and residuals (right) for Epoch V, from which the master reference images were derived for subsequent alignment. *To be replaced with newer figure?*



(b) The residuals of the pointing model. Note the Gaussian distribution.

Fig. 9.— Pointing model.

makes predictions about the observed timestreams, namely $d = Am$; this will be denoted $T[m] = d$.

The goal is to produce a time series for each bolometer which as closely as possible approximates $s + \varepsilon$ so that we may produce the best estimate of the astrophysical signal $m = M[s + \varepsilon] = S + N$.

We proceed iteratively as follows.

$$\tilde{a}^{(n)}(t) = \sum_i d_i(t) - \tilde{s}_i^{(n)}(t) - \tilde{e}_i^{(n)}(t) \quad (5)$$

where $\tilde{s}_i^{(0)}(t) = 0$. This mean atmosphere model is then fit to each bolometer to obtain the relative gains (flat field) of the detectors

$$\tilde{a}_i^{(n)}(t) = \frac{d_i(t) \cdot a(t)}{d_i(t)^2} a(t) = r_i a(t) \quad (6)$$

This is illustrated in Figure 6. The instrument errors, which are typically smaller than the atmosphere, are then estimated

$$\tilde{e}_i^{(n)}(t) = \text{somemodels} \quad (7)$$

and both the atmosphere and instrument models are subtracted from the raw time series

$$d_i(t) - \tilde{a}_i^{(n)}(t) - \tilde{e}_i^{(n)}(t) \approx s_i(t) + \varepsilon_i(t) \quad (8)$$

This is the best estimate of signal plus irreducible noise at iteration step n , and is made into a map

$$M[d_i(t) - \tilde{a}_i^{(n)}(t) - \tilde{e}_i^{(n)}(t)] = \tilde{m}^{(n)} \quad (9)$$

The current best map $\tilde{m}^{(n)}$ is then deconvolved to provide a relatively low-noise, smooth map from which to generate a timestream

$$T[\mathcal{D}[\tilde{m}^{(n)}]] = \tilde{s}_i^{(n)}(t) \quad (10)$$

We note that it is possible to produce an “error map”

$$N = M[d_i(t) - \tilde{s}_i^{(n)}(t) - \tilde{a}_i^{(n)}(t) - \tilde{e}_i^{(n)}(t)] \quad (11)$$

The process then begins again with Equation 5.

5.1. Atmosphere Fluctuation Noise Model

The simplest model for the atmosphere fluctuations makes use of the fact that the beams for all of the detectors pass through a nearly identical atmosphere, thus implying that atmosphere fluctuations will be highly correlated between detectors.

5.2. Instrument Error Signals

Most of the instrument error signals have characteristic features which allow them to be identified, though not always removed. The error signals include the following:

1. Pickup from the 60 Hz AC power. This appears as narrow lines in the PSD of the data. The second harmonic of 60 Hz is aliased via beating against the 130 Hz bolometer bias frequency into 10 Hz with sidebands split at ~ 1 Hz.
2. Spikes in voltage due to cosmic ray strikes on the bolometers (“glitches”).
3. Microphonic pickup due to vibrations of the receiver. The most noticeable microphonics occur at the end of each scan when the telescope is turning around and the field rotator is adjusting. This leads to broad spikes in the time series, whose long decay must be removed from the data, particularly during the beginnings of scans.

Fortunately, most of the AC powerline pick-up occurs at frequencies where there is no astrophysical signal, given the beam size and scan speed. Thus this error is dealt with by first notch filtering at the line frequencies and then low-pass filtering the data. Because of the low correlation with astrophysical signal, this step is performed only once and is not iterated.

Both glitches and microphonic pickup from the scan turnarounds are degenerate with astrophysical signal and must be estimated as part of the iterative process. Glitches are identified as large excursions from the RMS level after subtraction of the best atmosphere and bright source model, and the data there is excluded from inclusion in subsequent maps. The turnaround microphonics are modeled as decaying exponentials at the beginnings and ends of scans.

5.3. Data Flagging

Due to the large volume of data generated by the survey, it was necessary to develop new tools to quickly visualize the data and ensure data quality. We used a “waterfall”

An automated flagger was also created that flags out outlier data on a per-pixel basis. In order to make a robust measurement of the variance of the fluxes assigned to each pixel, we used the median average deviation over the data in the pixel and rejected high and low outliers at the 3-sigma level. Pixels with too little data to compute a deviation, i.e. those with < 3 data points, were also flagged out - these scan-edge pixels are the dominant contribution to the total number of flagged data points.

5.4. Creation of the Astrophysical Model

WRITTEN POORLY: The timestream data is made into a spatial map using the pointing data corresponding to each time point for each bolometer. The data is weighted by inverse variance across a single scan and then drizzled into a map with 7.2'' pixels using a nearest-neighbor algorithm. The nearest-neighbor matching allows the map to be returned to a timestream in the same manner, but with the S/N improved by averaging over all hits on a given pixel.

6. Noise and Systematic Effects

The error maps produced by the iterative mapping provide a natural way of estimating the systematic error resulting from imperfect subtraction of bright sources. This results in “ghosts” of the bright sources in the error maps E .

In some fields, flux from certain source spread out over the course of the iterative process using certain kernel sizes. The cause of this artifact are not yet well-understood, but using a different kernel size was an effective workaround and did little to change the properties of the final map.

The noise is correlated between adjacent pixels.

The final per-pixel error estimate is given as ...

Because observing conditions varied widely during the survey, the RMS noise levels obtained in the various fields of the BGPS also varies.

The depth can be converted into an estimate of mass via standard estimates.

7. Photometry

To do accurate and meaningful photometry on the Bolocam maps requires a good estimate of the noise (Section 6) but also an understanding of the spatial filtering imposed by the observing strategy and the cleaning and mapping of the data.

The Bolocam maps produced are the convolution of the (nearly Gaussian) primary beam $G(\mathbf{x})$, together with an effective high-pass spatial filter $F(\mathbf{x})$,

$$M'(\mathbf{x}) = (G(\mathbf{x}) \otimes F(\mathbf{x})) \otimes M(\mathbf{x})$$

The effect of the high pass filter is that the effective PSF $B = G \otimes F$ has the non-intuitive

property that its area is *zero*:

$$\int B(\Omega) d\Omega = 0$$

Clearly, this complicates the definition of surface brightness, and also imposes a limit on the size of features for which photometry may be meaningfully performed.

Figure 16 shows the fraction of flux recovered in the map as a function of source size for a range of different PCA components subtracted in the cleaning. These measurements were produced by inserting simulated gaussian sources at a range of peak flux densities and sizes spread out through the map and summing the flux in an ellipse on the final cleaned map. The median fraction over all sources of a given size is plotted in the figure.

Real data with the astrophysical source model removed were used as the background. Because this is real data, at lower numbers of PCA components subtracted, the atmosphere still dominates the total measured flux, which is particularly evident for the largest sources.

Figure 17 shows the fraction of flux recovered in the maps as a function of the deconvolution kernel used to create the astrophysical model maps. The differences at large source sizes are not yet well-understood (!!!!!), but at the smallest source size, it is evident that a deconvolution kernel smaller than the source size does not fully recover the source flux. Therefore we chose a deconvolution kernel smaller than the beam but larger than the pixel size used. Figure 13 demonstrates the effects of using both too large and too small a kernel.

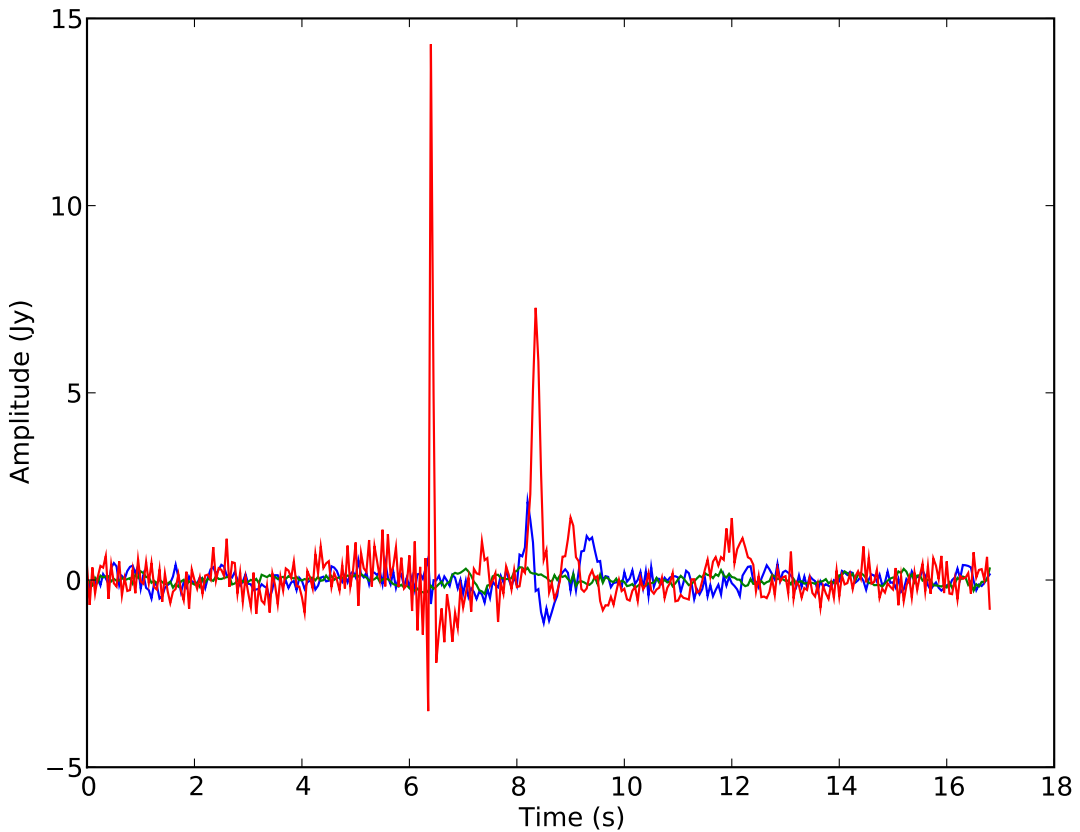


Fig. 10.— An illustration of a “glitch” in a single bolometer timestream (red) due to a cosmic ray strike. Note the acausal ringing due to the application of the downsampling filter. The time series for a physically adjacent bolometer is shown in blue, and a bolometer which does not pass over a source in green. The PCA model has already been subtracted from the data.

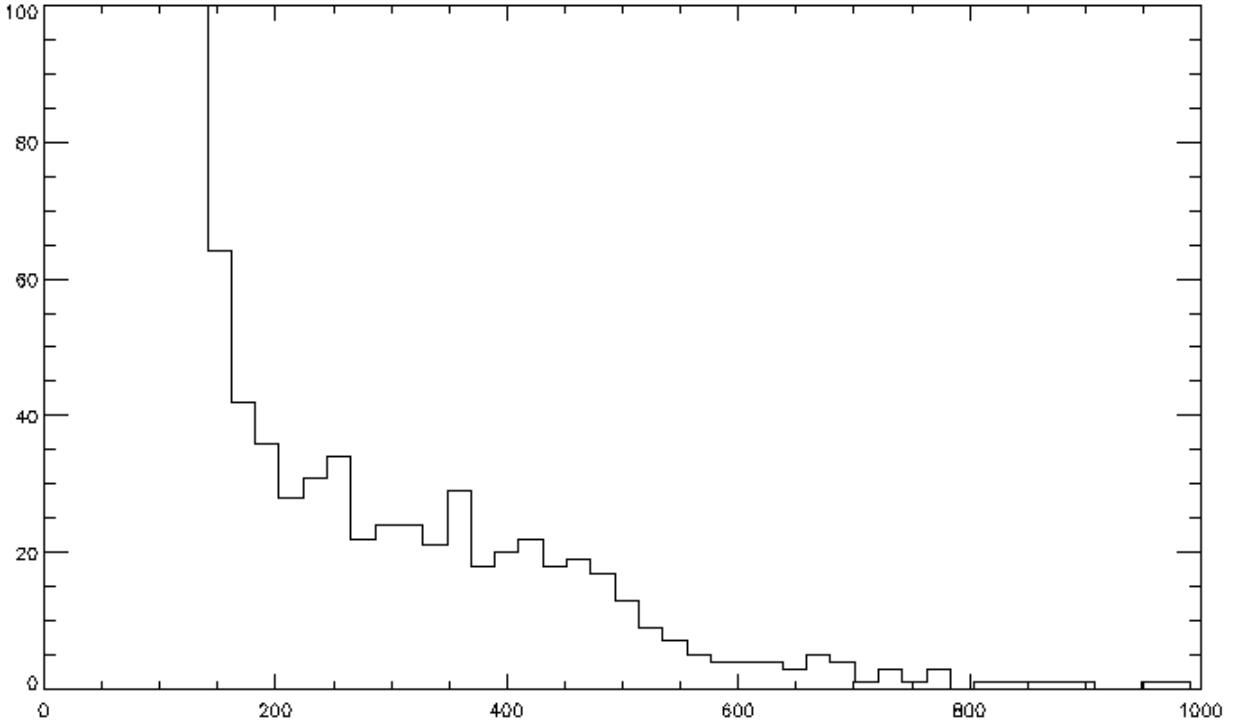


Fig. 11.— The distribution of glitch amplitudes flagged and removed from the data. The expected contribution to the noise from the unremoved glitches below the detection threshold is **TBD**.

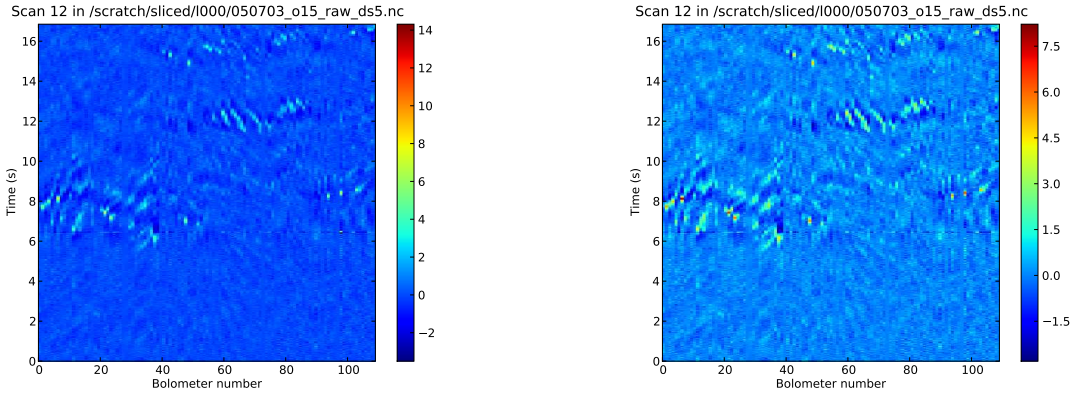


Fig. 12.— An illustration of the flagging process using the waterfall plot. Left: The glitch apparent at middle right is the same one whose time series is shown in Figure 10. Because of the PCA subtraction, the effect of the glitch also propagates over the other bolometers, appearing as a horizontal stripe. Right: The same data displayed with the time point including the glitch flagged out and rescaled

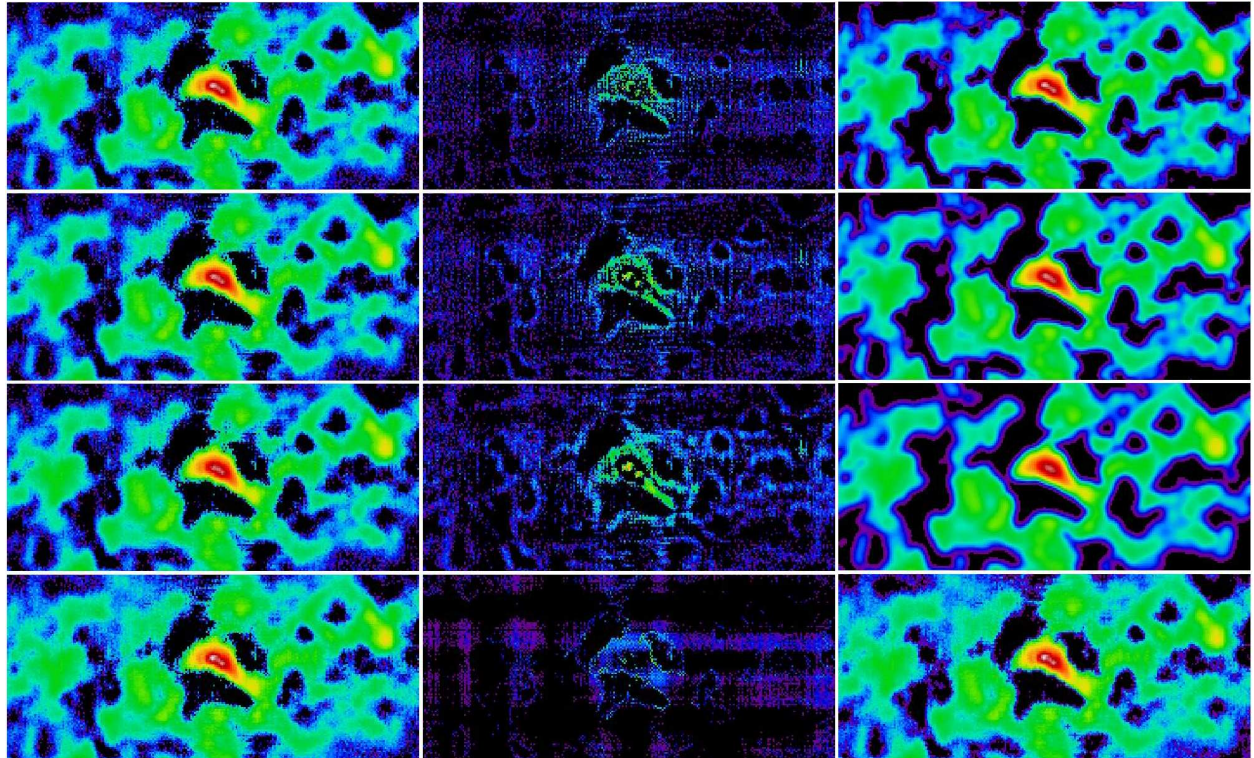


Fig. 13.— The effect of deconvolution on the iterative process can be seen in its effect on the residuals. From left to right: map, noise, smoothmap, model. Top to bottom kernel size: 14.4'', 21.6'', 31.2'', 7.2''. The final version of the pipeline uses 14.4'', which has the result of leaving no flux in the residual at the location of Sgr B2, and does not “dig a hole” in the residual map, as the 7.2'' kernel does.

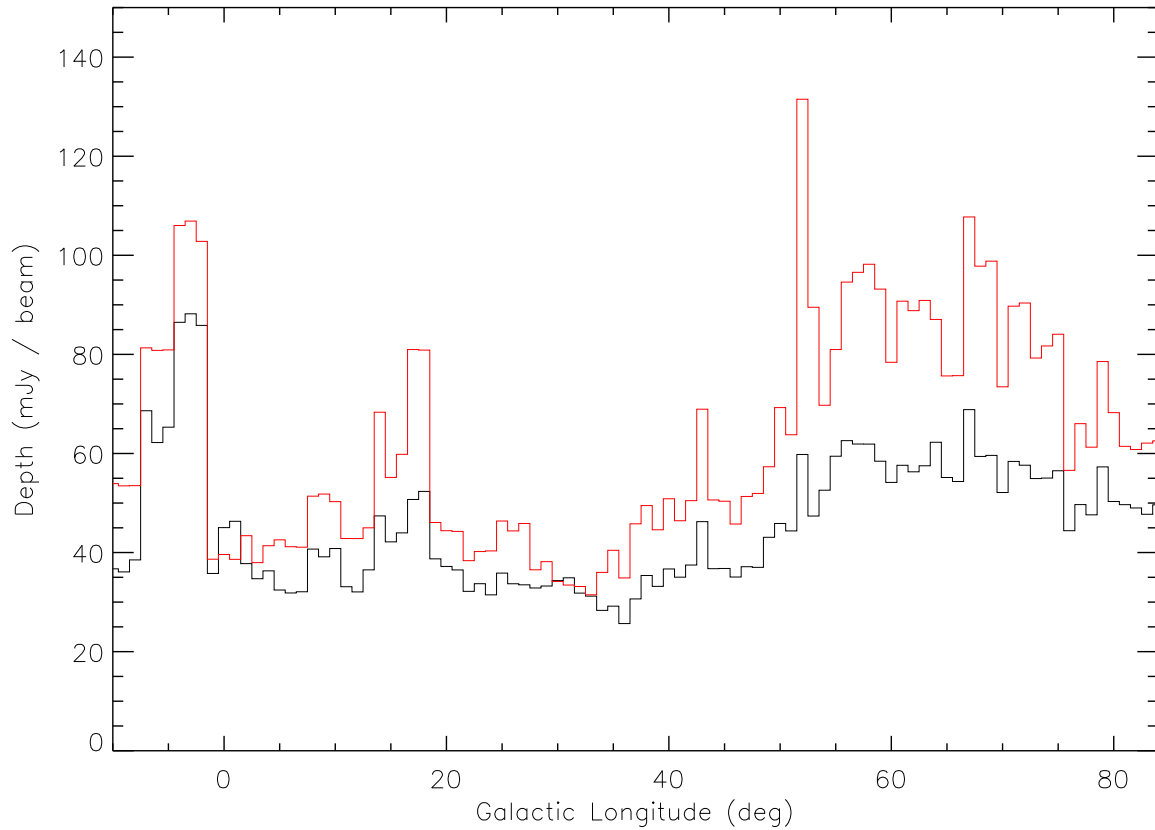


Fig. 14.— The depth of the BGPS in the first quadrant as a function of Galactic longitude. Black is the standard deviation of $0.9^\circ \times 0.9^\circ$ degree blocks centered on $b = 0$ and the longitude indicated; red is similar, but the estimator is $\text{median}(1/\sqrt{\text{weight map}})$.

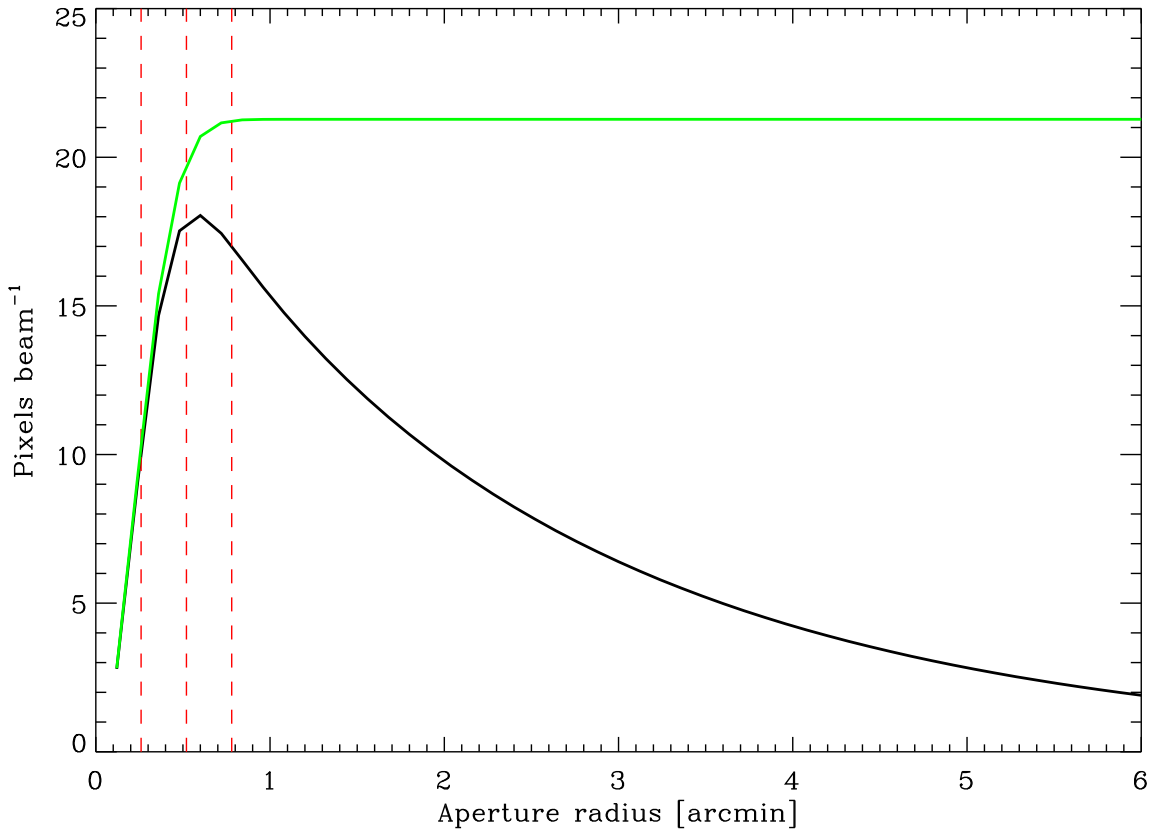


Fig. 15.— The effect of performing aperture photometry on a point source of unit flux observed with the effective Bolocam PSF B . The black curve shows the area (measured in pixels) as a function of the aperture radius for the filter measured via simulation. This is compared to the equivalent case for a Gaussian beam (green). The vertical lines show radii of $n/2 \times FWHM$ for $n = 1, 2, 3$. One can see that the Gaussian beam has nearly reached a constant area of $2\pi\sigma^2$ by a radius of $3/2 \times FWHM$, at which point any larger aperture would recover the full flux of the source. The actual Bolocam beam reaches its maximum effective area sooner, and then drops precipitously as the size of the aperture is increased.

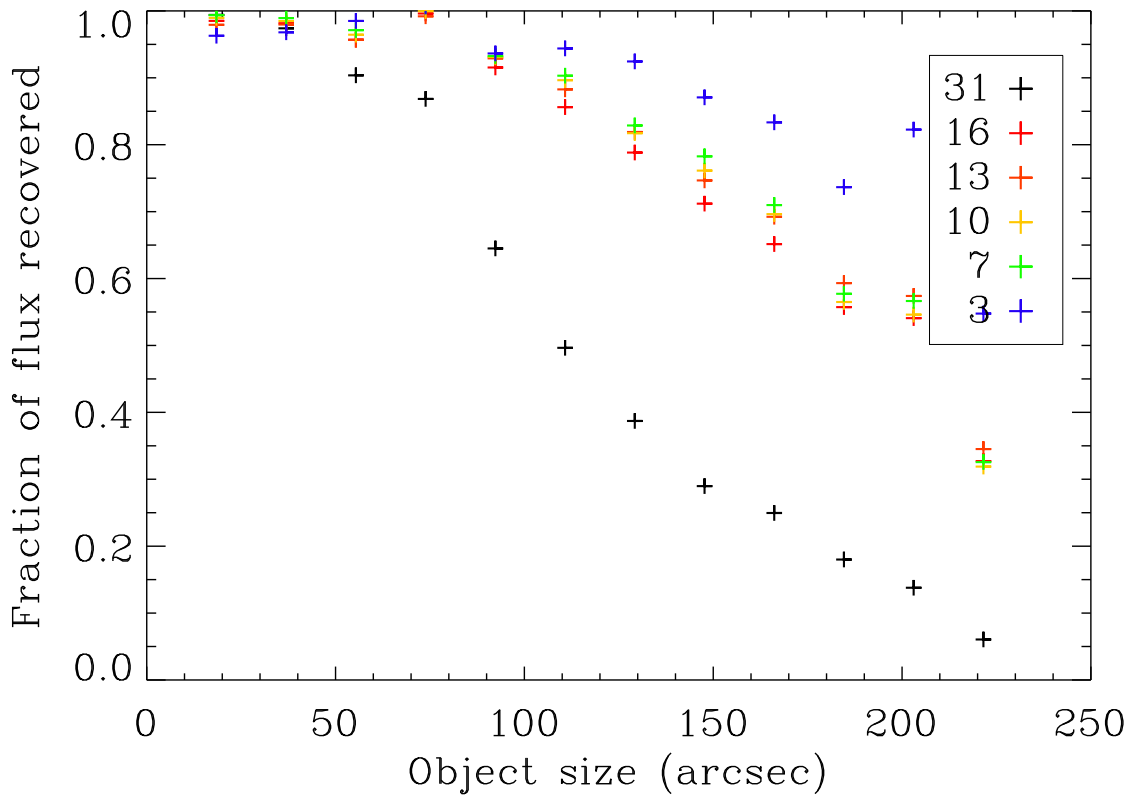


Fig. 16.— The fractional flux lost as a function of source size for well-separated Gaussian sources with the FWHM as indicated. Legend: number of PCA components

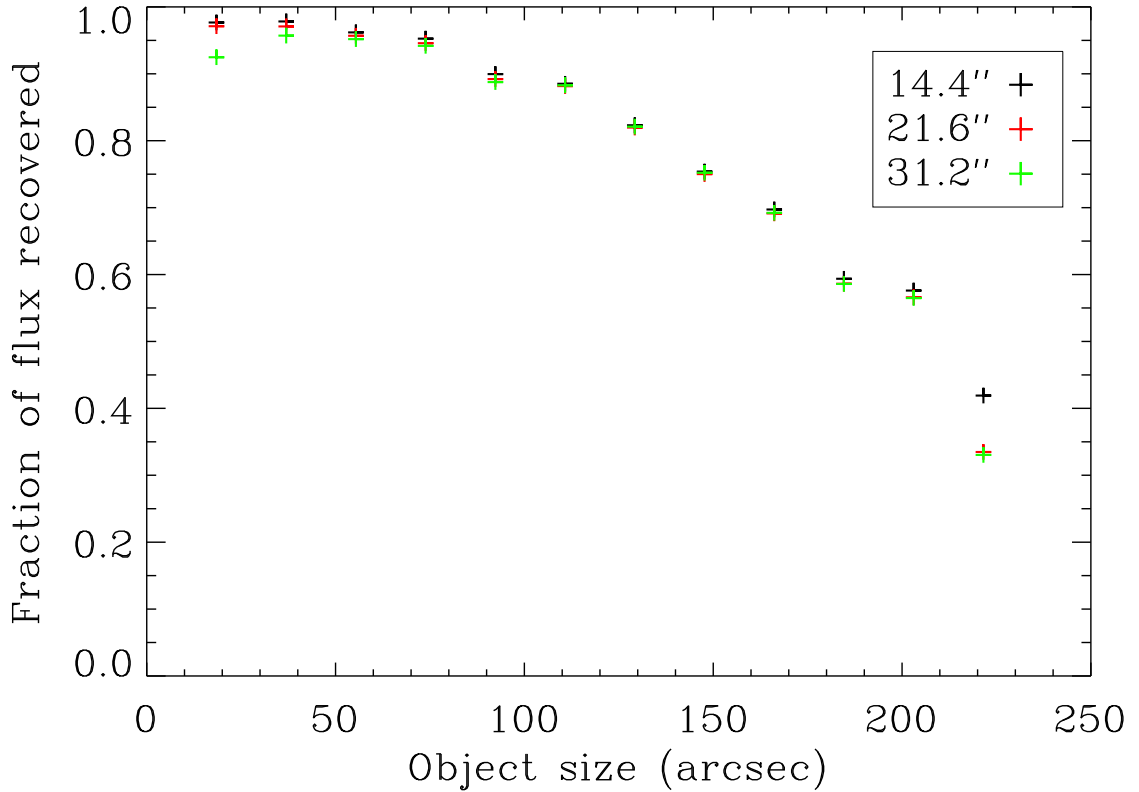


Fig. 17.— The fractional flux lost as a function of source size for well-separated Gaussian sources with the FWHM as indicated. Legend: Size of deconvolution kernel used to make model

8. Final Maps

The final maps are produced by coadding all observations of a single square degree centered on a particular Galactic coordinate (l_0, b_0) . The maps are made in Galactic coordinates using a plate carré (FITS header CAR) projection. As these maps are near the coordinate system equator, the difference between truly equiareal pixels and the pixels used is at most X%. The pixel size is $7.2''$, chosen to be much smaller than the Bolocam beam, and producing data squares 500 pixels on a side.

Noise maps are produced for each map, containing ...

9. Public Data Release

All processed maps are made available through IPAC².

10. Summary

The BGPS is the first (sub)millimeter survey of a substantial fraction of the Galactic Plane, providing an unbiased look at the high-density gas most intimately associated with the earliest phases of star formation.

We would like to acknowledge the staff and day crew of the CSO for their assistance. The BGPS project is supported by the National Science Foundation through NSF grant AST-0708403. J.A. was supported by a Jansky Fellowship from the National Radio Astronomy Observatory (NRAO). The first observing runs for BGPS were supported by travel funds provided by NRAO. Support for the development of Bolocam was provided by NSF grants AST-9980846 and AST-0206158. Team support was provided in part by NSF grant AST-0607793 to the University of Texas at Austin.

We recognize and acknowledge the cultural role and reverence that the summit of Mauna Kea has within the Hawaiian community. We are fortunate to conduct observations from this mountain.

Facilities: CSO (Bolocam)

A. Calculation of Color Corrections

If an experiment has finite bandwidth ($t(\nu) \neq \delta(\nu - \nu_c)$), to report a source surface brightness at a single frequency, one must assume a source spectrum. The power detected from that source is assumed to be

$$P_{in} = \eta A\Omega \int I_0(\nu)t(\nu)d\nu \quad (\text{A1})$$

(Here η and $A\Omega$ are the optical efficiency and throughput of the instrument, $I_0(\nu)$ is the nominal (assumed) surface brightness of the source, and $t(\nu)$ is the bandpass transmission

²<http://irsa.ipac.caltech.edu/Missions/bolocam.html>

normalized to 1.0 at its peak.) The effective band center ν_c is usually chosen such that

$$I_0(\nu_c) \simeq \frac{\int I_0(\nu)t(\nu)d\nu}{\int t(\nu)d\nu} \quad (\text{A2})$$

The band centers for Bolocam are calculated assuming a Rayleigh-Jeans (RJ) source spectrum

$$\begin{aligned} I_0(\nu_c) &= I_{RJ}(\nu_c) \\ &= \tau 2kT \frac{\nu_c^2}{c^2}, \end{aligned} \quad (\text{A3})$$

where τ is the optical depth of the source and k is Boltzmann's constant. Since the detected power is assumed to be

$$P_{in} = \eta A\Omega \int \tau 2kT \frac{\nu^2}{c^2} t(\nu)d\nu, \quad (\text{A4})$$

we can write

$$I_0(\nu_c) = \frac{P_{in}}{\eta A\Omega \int \nu^2 t(\nu)d\nu} \nu_c^2 \quad (\text{A5})$$

Now if we assume a different source spectrum, for example a greybody with power-law emissivity, the assumed input power is

$$\begin{aligned} P_{in} &= \eta A\Omega \int I_{GB}(\nu)t(\nu)d\nu \\ &= \eta A\Omega \int \tau(\nu_0)(\nu/\nu_0)^\alpha B_\nu(T)t(\nu)d\nu \end{aligned} \quad (\text{A6})$$

and the source spectrum inferred from the detected power is

$$\begin{aligned} I_{GB}(\nu_c) &= \tau(\nu_0)(\nu_c/\nu_0)^\alpha B_{\nu_c}(T) \\ &= \frac{P_{in}}{\eta A\Omega \int \nu^\alpha B_\nu(T)t(\nu)d\nu} \nu_c^\alpha B_{\nu_c}(T) \\ &= \frac{\int \nu^2 t(\nu)d\nu}{\int \nu^\alpha B_\nu(T)t(\nu)d\nu} \nu_c^{\alpha-2} B_{\nu_c}(T) I_{RJ}(\nu_c) \\ &\equiv \frac{I_{RJ}(\nu_c)}{K}. \end{aligned} \quad (\text{A7})$$

This defines the color correction K to apply to the reported Bolocam flux from a source if the source is assumed to have a greybody spectrum with power-law emissivity.

We note that for an arbitrary experiment with bandpass $t(\nu)$ that reports its surface brightness measurements assuming a spectrum $I_0(\nu)$, the surface brightness assuming a

different source spectrum $I_1(\nu)$ is given by

$$\begin{aligned} I_1(\nu_c) &= I_0(\nu_c)/K \\ &= I_0(\nu_c) \frac{I_1(\nu_c)}{\int I_1(\nu)t(\nu)d\nu} \left[\frac{I_0(\nu_c)}{\int I_0(\nu)t(\nu)d\nu} \right]^{-1} \end{aligned} \quad (\text{A8})$$

B. Pointing Calculation

To calculate the position at which to point the telescope, the CSO antenna computer computes an alt/az derived from the RA/Dec J2000 (heliocentric) catalog position. It performs the following calculation:

1. Precess catalog coordinates to current epoch. The CSO by default stores catalog positions in B1950.
2. Add aberration and nutation corrections. This is the “requested apparent” RA and Dec reported by the antenna computer.
3. The equatorial coordinates are transformed to horizon coordinates using the current local apparent sidereal time.
4. A 11-term model (“C-terms”) based on the optical pointing of the telescope is then applied to A and Z along with t -terms (?), the tilt of the alidade, and a refraction correction to obtain the necessary mechanical pointing of the telescope to acquire the source.
5. The telescope then attempts to follow this track; the difference between the requested A, Z and the actual, measured angles of the encoders (a result of servo errors) are also reported.

The CSO antenna computer reports this pointing information, including geocentric RA/Dec, at a rate of 100 Hz. This time series, along with the field rotator encoder information from Bolocam is merged with the bolometer time series and aligned.

To calculate the pointing used in the map from the telescope inputs, the Bolocam software does the following:

1. Start with the reported α', δ' from the CSO. Remove aberration and nutation corrections. Precess from current epoch to J2000. This gives α, δ .

2. Apply the ΔA , ΔE terms to α, δ to account for the difference between commanded and actual positions of the telescope.

C. Table of Absolute Pointing Sources

The absolute reference frame for the BGPS pointing model was chosen from a selection of bright quasars near the Galactic Plane. Table 3 gives the pointing sources used for this purpose.

Table 3. Absolute Pointing Calibrators

Number	Alias	RA(J2000)	Dec(J2000)	l	b	Flux (Jy)
1	1622-253	16 25 46.9	-25 27 38.3	352.14	16.32	0.18
2	16293-2422	16 32 22.9	-24 28 35.6	353.94	15.84	8.40
3	1657-261	17 00 53.2	-26 10 51.7	356.70	9.75	0.07
4	NGC6334I	17 20 53.4	-35 47 1.7	351.42	0.64	2.50
5	NRAO530	17 33 02.7	-13 04 49.5	12.03	10.81	2.70
6	1741-038	17 43 58.8	-3 50 4.6	21.59	13.13	1.44
7	1749+096	17 51 32.8	9 39 0.7	34.92	17.65	2.70
8	G5.89	18 00 30.4	-24 04 0.5	5.89	-0.39	3.57
9	M8E	18 04 53.0	-24 26 39.4	6.05	-1.45	3.92
10	G10.62	18 10 28.7	-19 55 49.8	10.62	-0.38	17.20
11	1830-211	18 33 39.9	-21 03 40.0	12.17	-5.71	1.70
12	G34.3	18 53 18.6	1 14 58.3	34.26	0.15	31.30
13	1908-202	19 11 09.6	-20 06 55.0	16.87	-13.22	1.00
14	G45.1	19 13 22.1	10 50 53.4	45.07	0.13	3.70
15	OV236	19 24 51.0	-29 14 29.8	9.34	-19.61	8.60
16	1923+210	19 25 59.6	21 06 26.1	55.56	2.26	0.32
17	1954+513	19 55 42.7	51 31 48.6	85.30	11.76	0.60
18	CYGA	19 59 28.5	40 44 1.7	76.19	5.75	0.25
19	K3-50	20 01 45.7	33 32 43.5	70.29	1.60	8.45
20	2005+403	20 07 44.9	40 29 48.6	76.82	4.30	0.40
21	ON1	20 10 09.1	31 31 37.7	69.54	-0.98	2.90
22	2013+37	20 15 28.7	37 10 59.6	74.87	1.22	1.40
23	2021+317	20 23 19.0	31 53 2.4	71.40	-3.10	0.54
24	2023+336	20 25 10.8	33 43 0.3	73.13	-2.37	0.92
25	GL2591	20 29 24.7	40 11 18.9	78.89	0.71	2.07
26	MWC 349	20 32 45.5	40 39 36.7	79.64	0.47	1.67
27	W75N	20 38 36.4	42 37 34.5	81.87	0.78	4.46
28	3C418	20 38 37.0	51 19 12.7	88.81	6.04	0.62
29	CRL 2688	21 02 18.8	36 41 37.7	80.17	-6.50	1.90
30	NGC7027	21 07 01.6	42 14 10.2	84.93	-3.50	9.27
31	2201+315	22 03 15.0	31 45 38.4	85.96	-18.78	0.35

Table 3—Continued

Number	Alias	RA(J2000)	Dec(J2000)	l	b	Flux (Jy)

D. Table of Reference Sources

Table 4. In-plane Millimeter Sources

Number	Alias	RA(J2000)	Dec(J2000)	l	b	Flux (mJy)
l351pps		17 23 50.2	-36 38 58.8	351.04	-0.34	-999.0
l354pps		18 00 50.0	-23 20 33.0	6.55	-0.10	-999.0
l357pps		17 40 57.3	-31 10 48.0	357.56	-0.32	-999.0
l000pps		17 46 37.1	-29 10 21.5	359.91	-0.31	-999.0
l000pps2		17 47 10.3	-28 46 11.8	0.32	-0.20	-999.0
l002pps		17 50 36.3	-27 06 2.8	2.14	0.01	-999.0
l006pps		17 57 34.4	-23 58 12.0	5.64	0.24	989.0
l009pps		18 06 14.2	-20 31 58.0	9.61	0.19	1187.0
l009pps2		18 06 15.5	-20 32 8.0	9.61	0.19	1189.0
l012pps		18 10 50.5	-17 55 54.0	12.42	0.51	1205.0
l015pps		18 14 35.3	-16 45 45.0	13.87	0.28	1085.0
l015pps2		18 21 08.5	-14 31 48.0	16.58	-0.05	748.0
l018pps		18 25 42.0	-13 10 13.0	18.30	-0.39	1544.0
l020pps		18 28 09.9	-11 28 47.0	20.08	-0.13	1650.0
l021pps		18 30 34.0	-9 34 54.0	22.04	0.22	993.0
l023pps		18 34 54.6	-8 49 18.0	23.20	-0.38	1681.0
l024pps		18 36 05.1	-7 31 21.0	24.49	-0.04	1851.0
l025pps		18 36 16.7	-6 43 8.7	25.23	0.29	-999.0
l026pps		18 37 18.4	-6 38 38.4	25.41	0.10	-999.0
l026pps2		18 39 04.9	-6 24 23.6	25.82	-0.18	-999.0
l027pps		18 41 51.1	-5 01 48.0	27.36	-0.17	3478.0
l028pps		18 44 19.0	-4 40 52.0	27.95	-0.55	-999.0
l028pps2		18 42 51.8	-4 00 1.9	28.39	0.08	-999.0
l029pps		18 42 15.6	-3 34 44.5	28.70	0.41	-999.0
l028pps2		18 42 50.8	-3 59 46.1	28.40	0.09	-999.0
l033pps		18 52 25.1	0 14 53.0	33.26	-0.11	-999.0
l035pps		18 53 39.1	1 50 32.0	34.82	0.35	756.0
l037pps		18 59 10.0	4 12 10.0	37.55	0.20	1045.0
l038pps		19 01 53.2	4 12 51.0	37.87	-0.40	1487.0
l040pps		19 05 40.9	6 26 5.0	40.28	-0.22	1700.0
l042pps		19 10 33.5	9 08 7.0	43.23	-0.05	1247.0

Table 4—Continued

Number	Alias	RA(J2000)	Dec(J2000)	l	b	Flux (mJy)
l044pps		19 11 54.4	9 35 53.0	43.80	-0.13	1829.0
l044pps2		19 13 28.4	10 53 41.0	45.12	0.13	1999.0
l048pps		19 23 10.8	14 26 31.0	49.37	-0.30	1903.0
l050pps		19 23 11.1	14 26 34.0	49.37	-0.30	2088.0
l079pps		20 29 25.3	40 11 28.0	78.89	0.71	1390.0
l079pps		20 29 25.2	40 11 30.0	78.89	0.71	2014.0
l079pps2		20 31 13.3	40 03 33.0	78.99	0.35	790.0
l080pps		20 34 42.8	39 44 45.0	79.13	-0.37	1104.0
l080pps2		20 40 05.3	41 31 48.0	81.17	-0.11	961.0
l080pps		20 30 28.7	41 16 6.0	79.88	1.18	1024.0
l082pps		20 40 26.8	41 56 54.0	81.54	0.10	805.0
l110.5npps		23 05 10.7	60 14 50.6	110.11	0.05	-999.0
l111pps		23 15 31.5	61 07 39.7	111.62	0.38	-999.0
l134p1		02 29 02.8	61 33 31.2	134.28	0.86	-999.0
l134p1-2		02 27 06.9	61 52 20.8	133.95	1.07	-999.0
l134p1-3		02 27 02.4	61 52 32.9	133.94	1.07	-999.0
l135p1		02 34 45.1	61 46 23.0	134.83	1.31	-999.0
l136p15		02 50 08.4	61 59 56.7	136.38	2.27	-999.0
l137p15		02 29 03.2	60 43 26.9	134.59	0.08	-999.0
IC1396		21 40 11.5	58 16 11.7	99.93	4.21	-999.0
IC1396-2		21 36 36.8	57 30 50.0	99.07	3.97	-999.0
IC1396-3		21 35 38.4	57 26 40.5	98.93	4.00	-999.0
l189pps		06 08 50.1	21 38 19.0	188.94	0.87	-999.0
l189pps-2		06 08 49.7	21 38 5.7	188.95	0.87	-999.0
l192pps		06 12 51.5	18 00 39.3	192.58	-0.05	-999.0
l192pps-2		06 12 51.5	17 59 36.3	192.59	-0.05	-999.0
l192pps-3		06 12 50.1	18 00 35.8	192.58	-0.05	-999.0
l192pps-4		06 12 50.3	17 59 28.8	192.59	-0.06	-999.0
l192pps-5		06 07 43.9	20 39 29.6	189.67	0.17	-999.0

REFERENCES

- Enoch, M. L. et al. 2006, ApJ, 638, 293
- Glenn, J. et al. 2003, in Proc. SPIE, Vol. 4855, Millimeter and Submillimeter Detectors for Astronomy, 30
- Griffin, M. J. & Orton, G. S. 1993, Icarus, 105, 537
- Haig, D. J. et al. 2004, in Proc. SPIE, Vol. 5498, Millimeter and Submillimeter Detectors for Astronomy II., ed. J. Zmuidzinas, W. S. Holland, & S. Withington, 78
- Johnstone, D. & Bally, J. 2006, ApJ, 653, 383
- Motte, F., Bontemps, S., Schilke, P., Schneider, N., Menten, K. M., & Broguière, D. 2007, A&A, 476, 1243
- Nummelin, A., Bergman, P., Hjalmarson, A., Friberg, P., Irvine, W. M., Millar, T. J., Ohishi, M., & Saito, S. 1998, ApJS, 117, 427
- Orton, G. S., Griffin, M. J., Ade, P. A. R., Nolt, I. G., & Radostitz, J. V. 1986, Icarus, 67, 289
- Rosolowsky, E. et al. 2009, ApJ, in prep, 000, 000
- Yoshida, H. & Phillips, T. G. 2005, in IAU Symposium, Vol. 235, IAU Symposium, 245P–+
- Young, K. E. et al. 2006, ApJ, 644, 326